Journal of Petroleum Science and Engineering 208 (2022) 109380

Contents lists available at ScienceDirect

Journal of Petroleum Science and Engineering

journal homepage: www.elsevier.com/locate/petrol

Shale gas production from reservoirs with hierarchical multiscale structural heterogeneities

Jianwei Tian [a], Jishan Liu [a,*], Derek Elsworth [b], Yee-Kwong Leong [a], Wai Li [a], Jie Zeng [a]

[a] School of Engineering, The University of Western Australia, 35 Stirling Highway, WA, 6009, Australia
[b] Departments of Energy and Mineral Engineering and Geosciences, G3 Centre and EMS Energy Institute, The Pennsylvania State University, University Park, PA, 16802, USA

ARTICLE INFO

Keywords:
Multi-scale heterogeneity
Discrete fracture network
Fractal permeability
Gas adsorption
Fractal hydraulic fracture

ABSTRACT

Hydrofractured shale reservoirs exhibit a complex hierarchy of heterogeneous structures. Although the importance of hierarchical structures has long been recognised, the full control of scale-dependent heterogeneities on gas production remains ill-defined. We characterize reservoir structural heterogeneity at four hierarchical levels: (1) heterogeneous nanopore structure of the OM (Organic Matrix/Kerogen); (2) heterogeneous micro-structure of the IOM (Inorganic Matrix); (3) discrete structure of the NFNs (Natural Fracture Networks); and (4) discrete structure of the HFs (Hydraulic Fractures). A fractal approach is applied to characterize these internal structural heterogeneities for both the OM and IOM. These characterisations are incorporated into the constitutive relations defining transport within the OM and IOM. NFNs are generated by the Monte Carlo method while HFs are represented by a fractal tree-like network. A constitutive law for flow within a fracture is applied to both NFNs and HFs. Overall mechanical equilibrium and continuity of deformations are applied across these hierarchical systems comprising the shale reservoir while separate field equations for transport are derived for each structural system. The mass exchange between the individual structural systems is satisfied through source/sink terms compatibility of deformation enforced through boundary conditions and internal controls. The resulting multi-scale heterogeneous model is verified against the analysis of an idealised shale reservoir. Simulation results honor the ultimate recovery fractions and demonstrate the significant impacts of both hydraulic fracture and natural fracture heterogeneities on the evolution of recovery. The verified model is applied to a field case. The modelled gas production rate curve agrees well with field data for a reservoir in Barnett shale. Sensitivity studies confirm that heterogeneities at all scales are important but that their respective roles evolve separately during the history of gas production.

1. Introduction

Shale gas production has undergone tremendous development worldwide over the last two decades, largely due to breakthroughs in horizontal drilling and hydraulic fracturing (Shaffer et al., 2013). Reservoir stimulation by hydraulic-fracturing increases permeability of the reservoir and allows for the commercial extraction of the gas. Shale reservoirs are typically heterogeneous aggregates of organic matter, inorganic minerals and clays and with an interconnected pore system. The resident gas is variously stored (a) on the pore surfaces of organic matter and clay minerals in adsorbed form, (b) as free gas in nanopores and microfractures, and (c) as solid kerogen and in connate water in the dissolved form (Zhang et al., 2012). The proportion of adsorbed gas ranges from 20% to 80 %, which is highly dependent on the total content of organic carbon (TOC) (Lan, 2019; Wu et al., 2014). Artificially-generated multistage hydraulic fractures (HFs) provide flow paths which divide the shale reservoir into matrix and fracture zones. During shale gas production, gas desorbs from the pore surface of the shale matrix and typically flows first into natural fractures (NFs) and from there into the HFs. These gas flow behaviours and the corresponding permeability attributed various scales of macro-through micro-fractures and pores are substantially influenced by the heterogeneity at each length scale (Akkutlu et al., 2017; Akkutlu and Fathi, 2012). Therefore, accurate characterisation of the multiscale heterogeneity of the reservoir is a prerequisite for the accurate evaluation of shale gas production.

* Corresponding author.
E-mail address: jishan.liu@uwa.edu.au (J. Liu).

https://doi.org/10.1016/j.petrol.2021.109380
Received 27 October 2020; Received in revised form 2 August 2021; Accepted 13 August 2021
Available online 14 August 2021
0920-4105/© 2021 Elsevier B.V. All rights reserved.

The shale matrix is a blend of organic matter (OM) and inorganic matter (IOM). Pore sizes within the OM vary from a few nanometres to hundreds of nanometres (Yuan et al., 2017). These highly-developed micropores provide abundant adsorption sites for the hydrocarbon gas. By contrast, the pore sizes in the IOM vary from 10 nm to 100 μm (Naraghi and Javadpour, 2015), as apparent from extensive measurements by micro-computed tomography (μ-CT), scanning electron microscopy (SEMs), mercury intrusion porosimetry and low-temperature adsorption (Chen et al., 2016; Guo et al., 2015; Vafaie et al., 2015). Such measurements demonstrate that the pore size distribution (PSD) of the shale matrix follows fractal scaling (Bu et al., 2015; Yang et al., 2014, 2016). Additionally, the fractal dimensions of the PSD are observed to be positively correlated with TOC with higher levels of OM indicating a more heterogeneous pore structure (Li et al., 2016). Moreover, because flow regimes (viscous flow, Knudsen diffusion and surface diffusion) are highly dependent on pore diameter, according to the definition of the Knudsen number, the fractal dimensions of the PSD within the OM significantly affects both diffusivity and apparent permeability (Tian et al., 2019). Accordingly, fractal-based permeability models have been developed and applied to describe gas flow within the shale matrix (Cai et al., 2018; Geng et al., 2018; Sheng et al., 2016; Zheng et al., 2013).

Stochastic NFs and HFs at macroscale are two pivotal attributes of shale reservoir heterogeneity which provide the primary transport paths for gas depletion. The corresponding permeabilities of NFs and HFs are typically several orders-of-magnitude higher than the matrix permeability. Higher densities of NFs improve flow transfer area and decrease diffusion lengths within the reservoir. However, widely-used dual-continuum models (Barenblatt et al., 1960; Warren and Root, 1963) and subsequent multi-porosity, multi-permeability models (Bai and Elsworth, 2000; Bai et al., 1993; Wu et al., 2010) are typically based on the assumption that individual solution cells within the reservoir are homogeneous and isotropic–not accommodating their true heterogeneous and fractal characteristics. Correspondingly, to obviate this problem, various approaches, including the discrete fracture model (Mi et al., 2014), local grid refinement with unstructured grids (Jiang and Younis, 2015) and embedded discrete fracture model (Xue et al., 2019) are proposed to model the complex fracture network explicitly in numerical simulation, aiming to provide more accurate production forecasting. Moreover, the HFs that consist of primary fractures and induced fractures can also be characterized by the continuum-based and discrete fracture models. As a continuum-based approach, a multi-domain model is proposed to incorporate the complexity of the stimulated volume (Li et al., 2019, 2020). More ideally, a fractal tree-like branched network may be employed to characterize the topology of HFs (Nandlal and Weijermars, 2019; Tan et al., 2018; Wang et al., 2015, 2018), including accommodating constraints on geometry supplied by micro-seismic data (Fan and Ettehadtavakkol, 2017). In this, the configuration of the fracture network is correlated to the fractal controlling parameters and bifurcation ratio.

Porosity and permeability change dynamically with the evolution of effective stress due to reservoir depressurisation during gas production (Chen et al., 2019; Cui et al., 2018). Gas depletion increases effective stresses, compacting pores and especially compliant fractures and typically reducing permeability (Cao et al., 2016b). Conversely, gas desorption from matrix pores also causes matrix shrinkage, potentially increasing pore diameters and related permeability. Therefore, the apparent permeability of the shale matrix evolves as a result of the potentially complex competition between these two processes operating across a range of length scales.

Contemporary views of fluid storage and transport in shale reservoirs define controls on processes that operate over a spectrum of scales - from nano-to kilo-metre. However, the resultant impact of multiscale heterogeneities, from microscale OM and IOM to macroscale NFs and HFs, remain incompletely understood. In this study, a fractal approach is applied to characterize the PSD of the dual-continuum matrix (OM and IOM) and used to define a fractal-based permeability model. The fractal characteristics of the matrix are interfaced with explicit representation of NFs and HFs as a branched dendritic discrete fracture network (DFN) representing fractal characteristics at all scales. A mechanical equilibrium equation is applied to the whole reservoir system. This equation regulates the distribution of the total stresses throughout the reservoir. Under this framework, a multi-scale heterogeneous model of gas production is developed to represent hydrofractured shale reservoirs across the full scale of the reservoir.

2. Conceptual model

Production typically transports gas from the nanopores in the shale matrix, through the network of NFs into the artificially-generated HFs and then to the well (Fig. 1). Multiscale heterogeneity within the reservoir may be represented at nested scales using heterogeneous distributions of HFs and discrete NFs at field scale and of PSDs for the IOM and OM at core scale. Importantly, the inherent heterogeneity of the pore structure and artificial HFs must be appropriately characterised.

In the shale matrix, the pore diameter is an important factor that determines both the apparent permeability and the dominant flow regime. Effective-stress-dependent fractal permeability models have been used to investigate the impacts of a heterogeneous matrix structure on the evolution of coal permeability (Tian et al., 2019). We extend this to both the OM and IOM by separately described their PSDs using a fractal approach. The conceptual model for the fractal-based dual continuum is presented in Fig. 2.

In addition to a heterogeneous PSD in the matrix, the pre-existing natural fracture network (NFN) also affects gas transport and production. The gas discharged from the matrix flows through the NFN and then into the hydraulic fracture network (HFN). The orientation, length distribution and intensity of the stochastic NFNs are critical parameters to characterize the NFN. According to the analysis of fracture data sets (Barton, 1978; Bridges, 1975; Manzocchi, 2002), a lognormal distribution provides the best fit to trace lengths. Thus, we assume that the trace length of the shale NFNs conforms to a lognormal distribution and that fracture orientations and locations within NFNs are following a uniform distribution.

Hydraulic fracturing creates both primary and secondary HFs (Blanton, 1986; Chen et al., 2015; Sheng et al., 2019) and in some cases with an irregular form and slightly branched structure. We honor this observation by developing an HFN as a dendritic network of fractures

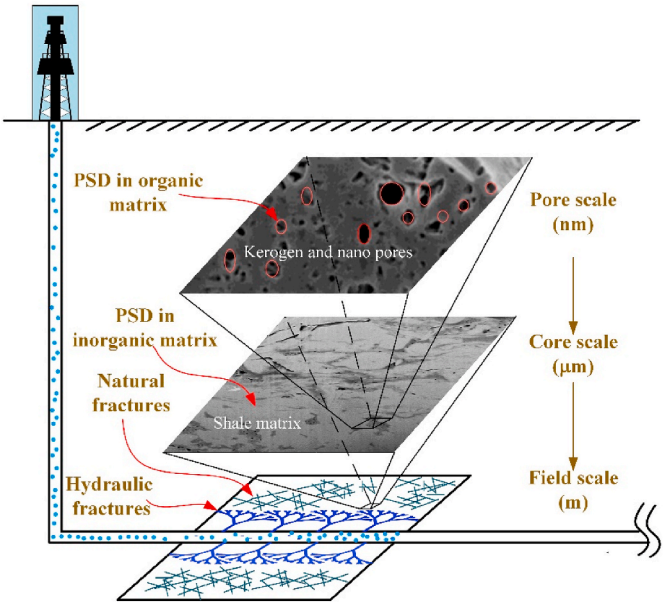

Fig. 1. Illustration of nested multiscale heterogeneities within a shale reservoir.

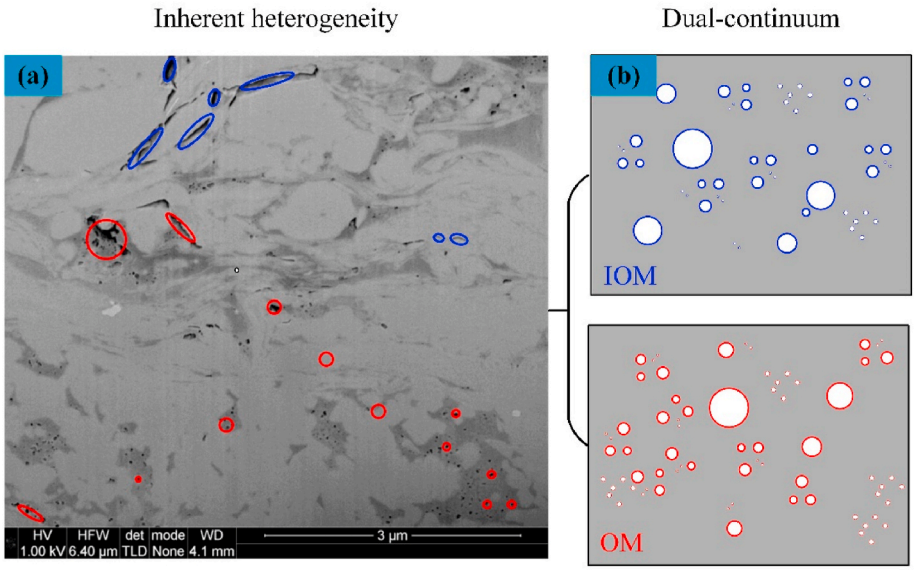

Fig. 2. Conceptual model for the PSD of OM and IOM: (a) SEM image of shale matrix (Ambrose et al., 2010); (b) Dual-continuum representation of OM and IOM.

with a fractal form, as displayed in Fig. 3. The fractal-based HFN is ideally based on the assumption that both fracture aperture and length follow a fractal scaling law. The orthogonal hydraulic fractures intersected with horizontal well are defined as primary HFs while the branched hydraulic fractures propagating from primary HFs are categorized as secondary HFs. Both the primary and secondary HFNs constitute the stimulated reservoir volume (SRV) with the region beyond the SRV representing an unstimulated reservoir volume (USRV) that remains pristine.

In addition to the hierarchical architecture of the pore structure within the reservoir, gas production involves complex nested feedbacks of multi-physics coupling process. These include principal couplings of gas desorption, shrinkage and flow in the OM, gas flow in the IOM, gas flow in NFN and HFN all overprinted by the impacts of changes in effective stress, as depicted in Fig. 4. Specifically, gas desorption and depletion in the kerogen induces shrinkage within the organic matter, which changes pore capillary diameters and intrinsic permeability. At the same time, pressure depletion and changes in effective stresses induce a transition in flow regimes and apparent permeability since both are highly dependent on pressure and pore diameter. In the IOM and fracture networks (NFN and HFN), a decrease in pore (fracture) pressure increases effective stress and potentially compacts fractures and reduces fracture apertures and related permeability. In summary, this sequential gas flow from OM to HFN is modulated by evolving effective stress and highly time-dependent. The following defines the governing equations for the hierarchy of the quadruple fields of sequentially nested media (OM, IOM, NF, HF) and the cross-coupling relationships among them.

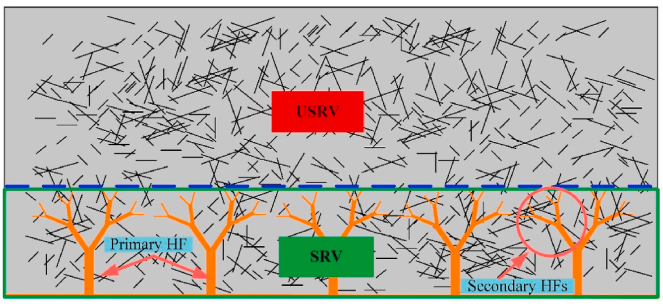

Fig. 3. Schematic of the conceptually ideal model for the fractally HFN and discrete NFN.

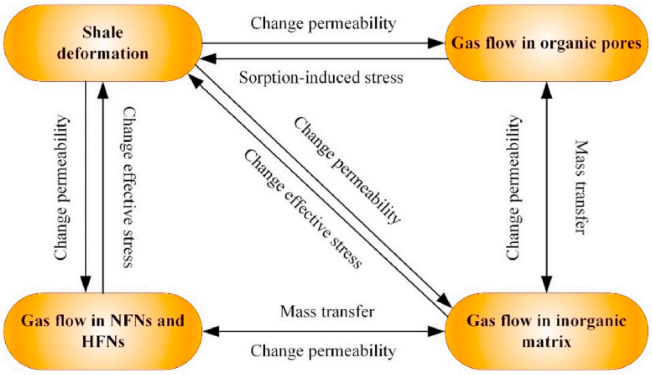

Fig. 4. Schematic of the cross-coupling relationships between different fields during shale gas production.

Coupling relations are either effective stress-dependent or pressure-dependent while mass exchanges are normally pressure and local rock structure-dependent. These relations are formulated and implemented into a finite element method-based PDE solver.

3. Formulation of the conceptual model

3.1. Formulation for shale deformation

The shale matrix comprises OM and IOM and is represented as a dual-porosity system with different flow and mechanical properties. Based on poroelastic response, the constitutive equation for matrix deformation is expressed as (Cao et al., 2016a; Zhang et al., 2008):

$$\varepsilon_{ij} = \frac{1}{2G}\sigma_{ij} - \left(\frac{1}{6G} - \frac{1}{9K}\right)\sigma_{KK}\delta_{ij} + \frac{\alpha_m p_m}{3K}\delta_{ij} + \frac{\alpha_k p_k}{3K}\delta_{ij} + \frac{\varepsilon_s}{3}\delta_{ij} \quad (1)$$

where $\varepsilon_{ij}$and$\sigma_{ij}$are the components of the total strain tensor and total stress tensor, respectively; $G$and $K$are the shear modulus and bulk modulus of the shale, respectively;$\sigma_{KK} = \sigma_{11} + \sigma_{22} + \sigma_{33}$ $\delta_{ij}$is the Kronecker delta; $\varepsilon_s$is the sorption-induced volumetric strain; α_m and α_k are the Biot coefficients of the IOM and OM, respectively, p_m and p_k are the gas pressure in IOM and OM in MPa, respectively. It is assumed that gas sorption occurs primarily in the OM system. Therefore, the sorption-induced swelling stress is dependent only upon the pore pressure of

the OM. The swelling strain is defined from the extended Langmuir equation as (Cui and Bustin, 2005; Zhang et al., 2008):

$$\varepsilon_s = \frac{\varepsilon_L p_k}{P_L + p_k} \tag{2}$$

where, ε_L is the Langmuir volumetric strain constant, P_L is the Langmuir pressure constant in MPa, and p_k is the pore pressure in the kerogen system. The Navier equation can be obtained by combining Eqs. (1) and (2), as follows:

$$Gu_{i,kk} + \frac{G}{1-2\nu} u_{k,ki} - \alpha_m p_{m,i} - \alpha_k p_{k,i} - K\varepsilon_{s,i} + f_i = 0 \tag{3}$$

where $u$is the displacement for shale under effective stress, f_i is the body force.

3.2. Formulation for gas flow in organic nanopores

Gas is present within the OM of the matrix in both adsorbed and free states. During gas depletion, gas transfers from the OM (kerogen) to the IOM as driven by the pressure differential. As pore diameters within the OM (kerogen) system span several orders-of-magnitude, gas transport is influenced substantially by variations in PSD. The mass balance equation for gas flow in the kerogen (OM) system is expressed as:

$$\frac{\partial m_k}{\partial t} + \nabla \cdot \left(-\rho_{gk} \frac{k_k}{\mu} \nabla p_k \right) = -Q_{mk} \tag{4}$$

where m_k denotes the total gas content in OM, which includes the free gas in nanopores and adsorbed gas in the OM, ρ_{gk} represents the density of free gas within the kerogen defined as an ideal gas as $\rho_{gk} = Mp_k/RT$ in kg/m^3, $k_k$is the permeability of the kerogen system and Q_{mk} on the right-hand side of the equation is the source term in kg/s. The current gas content can be defined as:

$$m_k = \rho_{gk}\varphi_k + \rho_{ga}\rho_s \frac{V_L p_k}{p_k + P_L} \tag{5}$$

where ρ_{gk} is gas density in the kerogen system at the corresponding pressure, φ_k is the porosity of the kerogen, ρ_{ga} is the gas density at standard conditions in kg/m^3, ρ_s denotes the density of the solid matrix, V_L denotes the Langmuir volume in m^3/kg, and P_L denotes the Langmuir pressure constant.

The majority of pores in the kerogen system are at nanometre-scale and the gas flow behaviour in these nanopores becomes flow-regime dependent. The Knudsen number (K_n) is defined as the ratio of the mean free path of the molecule relative to the pore diameter and is widely used to index flow regimes, as shown in Fig. 5 - indicating the relation among gas pressure, pore radius and K_n.

In the kerogen system (OM), the pore diameters of the nanoscale pores are of the same order as the mean free path of the gas (methane) molecule, enhancing the rate of collisions between the molecules and the pore walls and inhibiting transport. Gas flux is defined by the Knudsen diffusion equation with additional methane in the kerogen system adsorbed at the pore wall. Surface diffusion then occurs due to gas concentration differences on the nanopore walls. As shown in Fig. 6, viscous flow, Knudsen diffusion and surface diffusion all coexist in the nanopores of the OM, with each flow regime contributing to its apparent permeability.

The contribution ratio of viscous flow (C_v), contribution ratio of Knudsen diffusion (C_n) and contribution ratio of surface diffusion (C_s) to the total molar flux in OM are defined as:

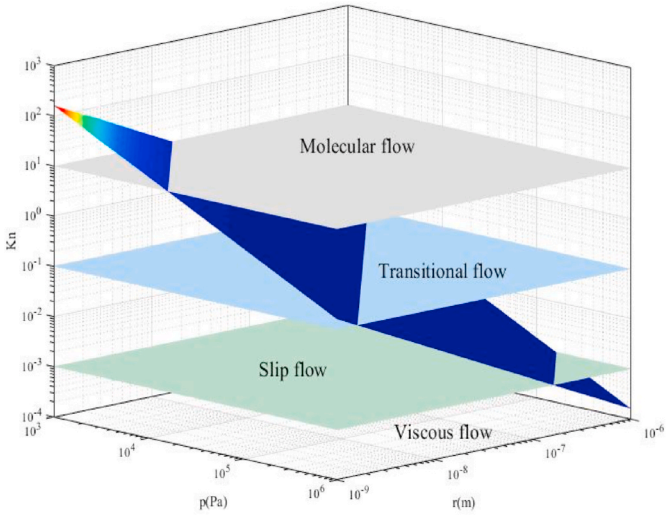

Fig. 5. Variation in Knudsen number classified against pore pressure and pore radius.

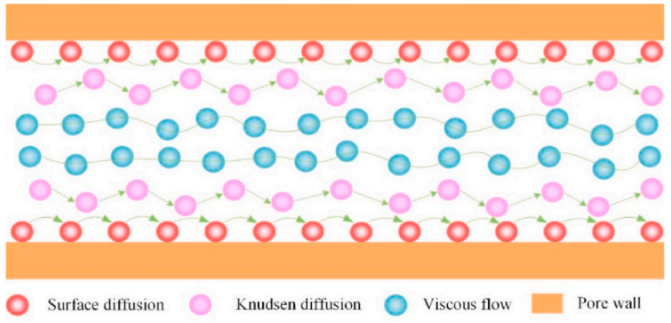

Fig. 6. Schematic illustration of flow regimes within a shale nanopore.

$$\begin{aligned} C_v &= \frac{Q_v}{Q_v + Q_n + Q_s} 100\% \\ C_n &= \frac{Q_n}{Q_v + Q_n + Q_s} 100\% \\ C_s &= \frac{Q_s}{Q_v + Q_n + Q_s} 100\% \end{aligned} \tag{6}$$

where the Q_v, Q_n and $Q_s$are the contributed molar flux of viscous flow, Knudsen diffusion and surface diffusion in mol (m^2/s).

The equivalent permeability of the OM is obtained as (see Appendix A):

$$k_k = k_v + k_n + k_s = \frac{\pi}{128} \frac{\varphi_k D_{ho}}{3 + D_{To} - D_{ho}} \frac{h_{maxo}^{3+D_{To}}}{L_{o0}^{D_{To}+1}} + \sqrt{\frac{2\pi RT}{M_g}} \frac{\varphi_k \mu D_{ho}}{(2 + D_{To} - D_{ho})} \frac{h_{\mathrm{max}o}^{2+D_{To}}}{6 p_k L_{o0}^{D_{To}+1}} + \frac{\pi D_s P_L C_{us} RT}{(p_k + P_L)^2 p_k} \frac{\mu D_{ho}}{(2 + D_{To} - D_{ho})} \frac{h_{\mathrm{max}o}^{1+D_{To}}}{L_{o0}^{D_{To}+1}} \tag{7}$$

where for the OM, D_{ho} is the fractal dimension of the PSD, which can be evaluated from$D_{ho} = 2 - \ln(\varphi_{k0}) / \ln(h_{\mathrm{mino}} / h_{\mathrm{maxo}})$, h_{maxo} is the maximum pore diameter, $h_{\mathrm{mino}}$is the minimum pore diameter, $D_{To}$is the fractal dimension of the tortuosity within the pores of OM, $L_{o0}$is the tortuous flow length of the pores in m, with D_s as the surface diffusion coefficient in m^2/s and C_{us} as the maximum concentration of adsorbed gas in mol/m^3. The first term in Eq. (7) represents the Darcy permeability, the second term represents the equivalent permeability due to Knudsen diffusion and the third term represents equivalent permeability due to

the surface diffusion. In the above equation, the primary variables are D_{ho} and h_{maxo}, which are correlated with porosity and effective stress (Tian et al., 2019) as:

$$\begin{cases} L_{o0} = \sqrt{\dfrac{\pi D_{ho} h_{\mathrm{maxo}}^2}{4\varphi_k(2-D_{ho})}\left[1-\left(\dfrac{h_{mino}}{h_{maxo}}\right)^{2-D_{ho}}\right]} \\ h_{maxo} = h_{maxo0}\sqrt{\left[1+\dfrac{\alpha_k}{\varphi_k}(S-S_0)+(\varepsilon_s-\varepsilon_{s0})-\dfrac{p_k-p_{k0}}{K_k}\right]\dfrac{2-D_{ho}^{'}}{2-D_{ho}}\dfrac{D_{ho}}{D_{ho}^{'}}\dfrac{1-\varphi_{k0}}{1-\varphi_k}} \end{cases} \tag{8}$$

where h_{mino} is minimum pore diameter within the OM in m, $D_{ho}^{'}$ is the fractal dimension under a given effective stress and $\varepsilon_v = \varepsilon_{11} + \varepsilon_{22} + \varepsilon_{33}$ denotes the volumetric strain of the shale, $S = \varepsilon_v + \frac{p_k}{K_s} - \varepsilon_s$, $S_0 = \varepsilon_{v0} + \frac{p_{k0}}{K_s} - \varepsilon_{s0}$. The evolution of porosity and pore diameter h within the OM (kerogen) under the influence of effective stress is calculated using the Cui-Bustin model (Cui and Bustin, 2005) as:

$$\varphi_k = \varphi_{k0}\exp\left(-c_k\left[\overline{\sigma}-\overline{\sigma}_0-(p_k-p_{k0})\right]\right) \tag{9}$$

where φ_{k0} is the initial porosity of OM, c_k stands for the compressibility of the OM in Pa^{-1}, $\overline{\sigma}$ and $\overline{\sigma}_0$ are mean total stress at current and initial state, respectively, and p_{k0} is the initial gas pressure in kerogen system.

3.3. Formulation for gas flow in the inorganic matrix

The mass balance equation for gas transport in the IOM is expressed as:

$$\frac{\partial m_m}{\partial t} + \nabla\cdot(\rho_{gm}\mathbf{q}_{gm}) = Q_{mk} \tag{10}$$

where m_m is the free gas content within the IOM, defined as $m_m = \rho_{gm}\varphi_m$, where ρ_{gm} represents the density of free gas within the IOM defined as an ideal gas as $\rho_{gm} = Mp_m/RT$, with Q_{mk} representing a source term for gas transfer between OM and IOM. According to the theory from Kazemi et al. (1992), the transfer rate may be determined as:

$$Q_{mk} = \frac{\alpha\rho_k k_k}{\mu}(p_k - p_m) \tag{11}$$

where α is the shape factor for the IOM defined as $\alpha = 8/L_k^2$(Kazemi, 1969) in m^2, L_k is the IOM spacing in m, k_k is the apparent permeability within the kerogen, ρ_k is the density of the solid kerogen.

This formulation assumes that the IOM experiences only viscous and slip flows and that the PSD adheres to a fractal distribution of pore sizes. The apparent permeability model that is used may be expressed as (Tian et al., 2019):

$$k_{\mathrm{m}} = \frac{\pi}{128}\frac{\varphi_m D_{hi}}{3+D_{Ti}-D_{hi}}\frac{h_{\mathrm{maxi}}^{3+D_{Ti}}}{L_{m0}^{D_{Ti}+1}}\left(1+\frac{8\mu(3+D_{Ti}-D_{hi})}{h_{\mathrm{maxi}}(2+D_{Ti}-D_{hi})}\sqrt{\frac{\pi R_g T}{2M_g}}\right) \tag{12}$$

where D_{hi} is the fractal dimension of the PSD in the IOM, defined as $D_{hi} = 2 - \ln(\varphi_m)/\ln(h_{\mathrm{mini}}/h_{\mathrm{maxi}})$, h_{maxi} is the maximum pore diameter within the IOM and D_{Ti} is the fractal dimension of pore tortuosity in IOM. In Eq. (12), the flow length L_{m0} of the REV for the two-dimensional case is defined as (Xu and Yu, 2008):

$$L_{m0} = \sqrt{\frac{\pi D_{hi} h_{\mathrm{maxi}}^2}{4\varphi_m(2-D_{hi})}\left[1-\left(\frac{h_{\mathrm{mini}}}{h_{\mathrm{maxi}}}\right)^{2-D_{hi}}\right]} \tag{13}$$

The porosity of the IOM under effective stress can also be calculated as (Cui and Bustin, 2005):

$$\frac{\varphi_m}{\varphi_{m0}} = \exp\left(-c_m\left[\overline{\sigma}-\overline{\sigma}_0-(p_m-p_{m0})\right]\right) \tag{14}$$

where φ_{m0} is the initial porosity of IOM, c_m is the compressibility of the IOM, and p_{m0} is the initial pore pressure in IOM.

The maximum pore diameter of the IOM (h_{maxi}) in Eq. (12) is determined from (Tian et al., 2019):

$$h_{\mathrm{maxi}} = h_{\mathrm{maxi0}}\sqrt{\left[1+\frac{\alpha_m}{\varphi_m}\left(\varepsilon_v-\varepsilon_{v0}+\frac{p_m-p_0}{K_m}\right)-\frac{p_m-p_0}{K_m}\right]\frac{2-D_{hi}^{'}}{2-D_{hi}}\frac{D_{hi}}{D_{hi}^{'}}\frac{1-\varphi_{m0}}{1-\varphi_m}} \tag{15}$$

where h_{maxi0} is the initial value of the maximum pore diameter within the IOM, $D_{hi}^{'}$is the fractal dimension under the acting effective stress and is correlated with IOM porosity and$\varepsilon_v = \varepsilon_{11} + \varepsilon_{22} + \varepsilon_{33}$ denotes the volumetric strain of IOM. As there is no adsorption in the inorganic matter (IOM), the adsorption-induced strain term is absent.

3.4. Formulation for gas flow within natural and hydraulic fractures

The network of discrete fractures is developed by randomly distributing NFs throughout the entire reservoir with lengths following a log-normal distribution. Hydraulic fracturing introduces HFs superimposed upon the NF network and increases connectivity between the primary fractures and induced secondary fractures. The pattern of the HFN is also assumed to conform to the dendritic fractal structure, as shown in Fig. 7. Both fracture length and aperture follow the fractal scaling law. The branching ratio used in this study is two, which means that $l_k = 2l_{k-1}$ and $d_k = 2d_{k-1}$. Both the NFN and HFN are assumed to be one-dimensional line conduits with aperture scaling with branch length.

Gas flux through the fracture conduit conforms to Darcy's law for the fracture as (Cao et al., 2016b):

$$\mathbf{q}_f = -\frac{k_f}{\mu}d_f\nabla_T p_f \tag{16}$$

where $\mathbf{q}_f$ is the rate of gas flow per unit thickness of the reservoir (2D) in m/s, d_f is the fracture aperture in m, k_f denotes the fracture permeability and $\nabla_T p_f$ is the pressure gradient in the longitudinal direction. Mass conservation within the fracture requires that (Cao et al., 2016b):

$$d_f\frac{\partial(\varphi_f\rho_f)}{\partial t} + \nabla_T\cdot(\rho_f\mathbf{q}_f) = 0 \tag{17}$$

where φ_f is fracture porosity and ρ_f is gas density. As the reservoir is depleted, the permeability of the fracture network decreases concomitantly with the increase in effective stress, with the evolution of fracture permeability represented as (Cao et al., 2016a; Li et al., 2020):

$$k_f = k_{f0}\exp\left(-c_f\left(p_{f0}-p_f\right)\right) \tag{18}$$

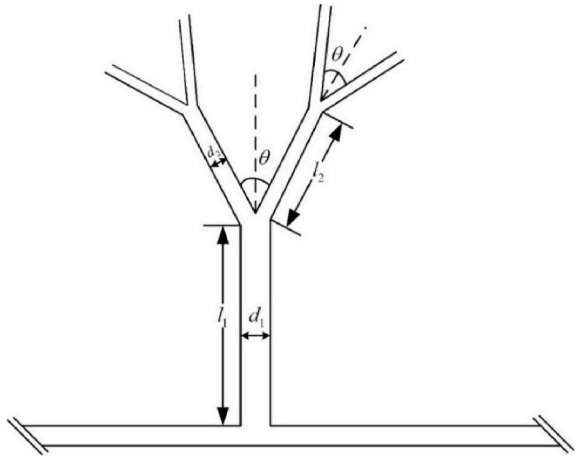

Fig. 7. Schematic illustration of a single multi-level branched HF.

where k_{f0} is the initial permeability of fractures and $c_f$is the compressibility of fractures.

4. Model verification

The previous governing equations represent a multi-scale heterogeneous system accommodating gas flow and mechanical deformation coupled across all scales and solved using the generic PDE solver COMSOL Multiphysics. The fractal-based OM and IOM are treated as dual-continuum media, while the HFs and NFs are explicitly represented as 1D conduit elements. We verify the proposed model using two different cases. Firstly, to demonstrate the embedded fracture network does not alter the recovery fraction, we verify the model by exploring the evolution of gas recovery fraction for an ideal reservoir with small dimensions. After that, a history matching of gas production rate for a reservoir in the Barnett shale is performed to verify the robustness of the model. The parameters used for both verifications are presented in Table 1, which are from the literature (Cao et al., 2016b; Geng et al., 2018; Yu and Sepehrnoori, 2014).

Table 1
Reservoir parameters used for model verification.

Parameters	Conceptual verification	Field verification	Unit
Reservoir dimensions	$40 \times 20 \times 5$	$550 \times 145 \times 90$	m
Original pressure	34.5×10^6	20.34×10^6	Pa
Maximum hotizontal stress	40	40	MPa
Minimum hotizontal stress	37	37	MPa
Temperature	352	352	K
Bottom hole pressure	2.4×10^6	3.69×10^6	Pa
Poisson's ratio	0.2	0.2	
Young's modulus	26	26	GPa
Bulk modulus of IOM	15	15	GPa
Bulk modulus of OM	8	8	GPa
Viscosity of gas	2×10^{-5}	2×10^{-5}	Pas
Langmuir pressure	3×10^6	4.48×10^6	Pa
Langmuir volume	2.5×10^{-3}	2.72×10^{-3}	m^2/kg
Biot coefficient of OM	0.054	0.054	
Initial porosity of OM	0.065	0.065	
Fractal dimension of PSD in OM	1.3	1.3	
Fractal dimension of OM tortuosity	1.4	1.4	
Minimum pore size of OM	1	1	nm
Maximum pore size of OM	50	50	nm
Compressibility of OM	7×10^{-10}	7×10^{-10}	Pa^{-1}
Biot coefficient of IOM	0.63	0.63	
Initial porosity of IOM	0.04	0.04	
Fractal dimension of PSD in IOM	1.3	1.3	
Fractal dimension of IOM tortuosity	1.4	1.4	
Compressibility of IOM	1×10^{-10}	1×10^{-10}	Pa^{-1}
Minimum pore size of IOM	1	1	nm
Maximum pore size of IOM	100	100	nm
IOM spacing	1×10^{-4}	1×10^{-4}	m
Compressibility of NFs	3×10^{-9}	1×10^{-8}	Pa^{-1}
Compressibility of HFs	2×10^{-9}	5×10^{-9}	Pa^{-1}
Initial NF permeability	30	1.5	mD
NF width	0.0005	0.0005	m
Number of NFs	400	500	
HF width	0.003	0.003	m
Number of primary HFs	7	28	
Bifurcate angle	40°	40°	°
Branching ratio	2	2	
Braching level	4	4	
Hydraulic fracture spacing	5	30	m
Initial HF permeability	500	100	mD
Half-length of primary HF	5	25	m
Surface diffusion coefficient	1×10^{-8}	1×10^{-8}	m^2/s

4.1. Verification of recovery fraction for an ideal reservoir

The flow model and mechanical model used for the verification of recovery fraction (RF) are illustrated in Fig. 8 (a) and Fig. 8 (b), respectively. It can noted that the NFN is not incorporated into the mechanical model. The model dimensions are 40m long, 20m wide, and 5m thick. The maximum horizontal stress (40 MPa) and minimum horizontal stress (37 MPa) are applied to the upper and right-side boundaries, respectively, with the facing boundaries with roller constraints. It should be noted that the fracture networks are not incorporated into calculating the evolution of stress filed. The intersection between the horizontal well and the primary hydraulic fractures are set at a bottom-hole pressure of 3.69 MPa. The other boundaries are set as no-flow boundaries. The initial reservoir pressure is 20.34 MPa. The fractal dimension of the OM and IOM are set as 1.3. There are a total of 400 NFs with a mean length of 4 m and variance of 1 m^2. All other parameters used in this verification are as listed in Table 1. The pressure difference between the reservoir and the horizontal well prompts gas recovery from the shale matrix to the wellbore. We performed three modelling cases: (1) a base case with NFs and induced secondary HFs, (2) a case without the induced secondary HFs (only the primary HFs are considered in the simulation), and (3) a case without NFs. As shown in Fig. 9, the recovery factors (RFs) for the three scenarios all eventually approach 0.7. This illustrates that the presence of NFs and HFs does not impact ultimate gas production but does affect the rate of recovery – production is significantly faster with NFs and HFs. The reason for this phenomenon is that the one-dimensional fracture networks does not alter the final porosity when the equilibrium state is achieved. For the base case, it takes 600 days to reach the ultimate gas production but 1600 days for the case without secondary HFs and 3000 days for the case without HFs, respectively.

4.2. Verification of gas production rate for barnett shale reservoir

Barnett shale has developed NFNs, which has been investigated in previous studies (Gale et al., 2014; Yaghoubi, 2019). Besides, Fan and Ettehadtavakkol (2017) upscaled the microseismic data of fracture network and found the induced fracture network can be described with fractal approach effectively. In addition to the induced hydraulic fracture, the pore size in Barnett shale matrix also exhibits fractal law (Ruppert et al., 2013). Accordingly, the proposed model is verified against field production data from the Barnett shale (Yu and Sepehrnoori, 2014). A single quadrant of the reservoir is selected to take advantage of the symmetry. A plan views of the flow and mechanical model with a dimension of 550m × 145m × 90m are presented in Fig. 10 (a) and Fig. 10 (b). There are 500 natural fractures in the entire domain with a mean length of 40m and variance of 100 m^2. In situ stress is applied to the upper and right boundaries as 40 MPa and 37 MPa respectively with an initial reservoir pressure of 20.34 MPa. The specific parameters used in the simulation are provided in Table 1. As shown in Fig. 11, the gas production rates derived from the numerical simulations of the Barnett shale were compared with the corresponding field data. It can be observed that a decline in the gas production rates of the Barnett shale varies from $2.5 \times 10^5 m^3$/day to $1.6 \times 10^4 m^3$/day over a production period of 1600 days – correlating strongly with field observations. Gas pressure distribution maps for the IOM after production periods of 100 days, one year, and ten years are presented in Fig. 12. In the first 100 days of gas production, the drainage area is primarily limited in the SRV and the gas pressure near the HFs exhibits a significant decline. By contrast, when the production period reaches 1 year, the gas pressure in the SRV is reduced to a half and the drainage area expands to the USRV. After 10 years, the gas in the SRV is almost fully depleted while the gas pressure in USRV is reduced to approximately half. Drainage of the gas in the USRV then proceeds over a much longer time than that in SRV.

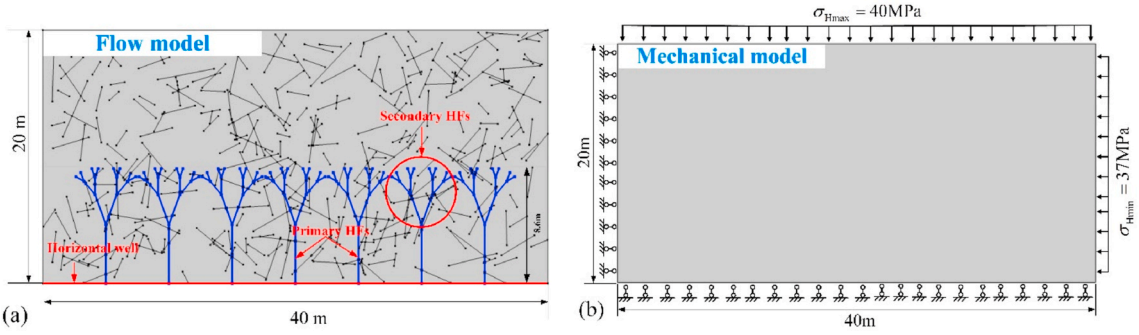

Fig. 8. Model verification of RF: (a) Flow model; (b) Mechanical model and boundary conditions.

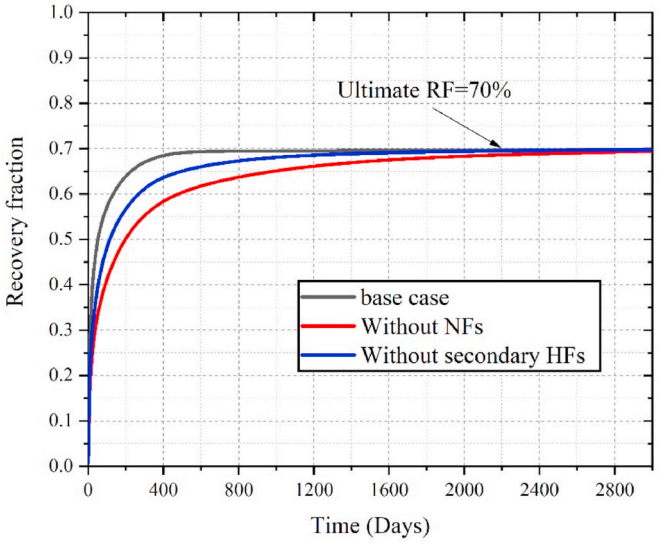

Fig. 9. Evolution of RFs for the three cases.

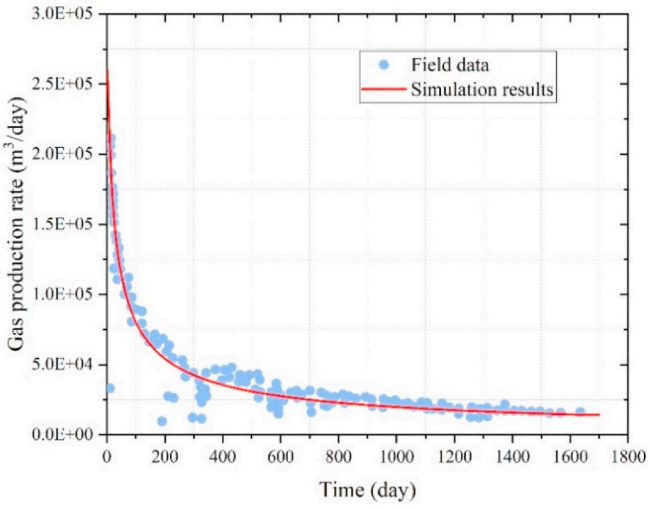

Fig. 11. History matching of Barnett shale production rate based on the proposed model.

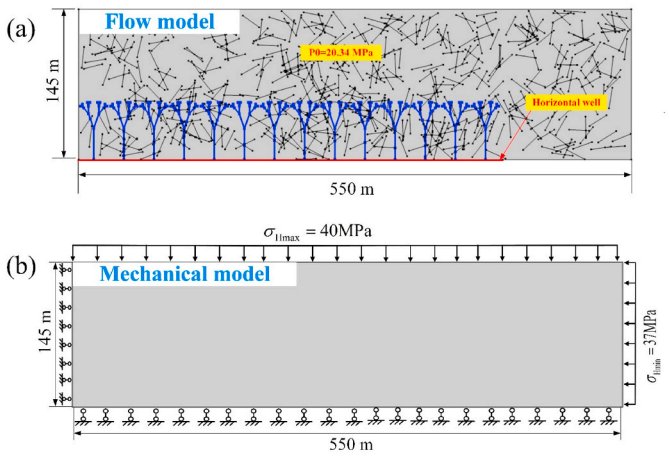

Fig. 10. Geometric model and boundary conditions for field verification.

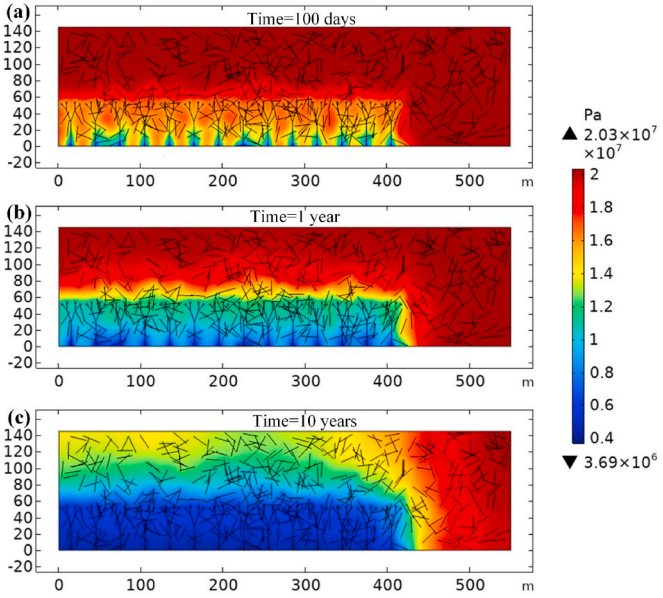

Fig. 12. IOM gas pressure distribution for Barnett shale for various production times: (a) 100 days; (b) 1 year; (c) 10years.

5. Impact of multiscale heterogeneities

The impacts of multiscale heterogeneities on the evolution of permeability and gas production may also be evaluated. We expand the numerical models used in the RF verification by × 10 to field scale with dimensions of 400 (length) × 200 (width) × 50 (thickness) m^3, as shown in Fig. 13 (a) and Fig. 13 (b). The boundary conditions are identical to

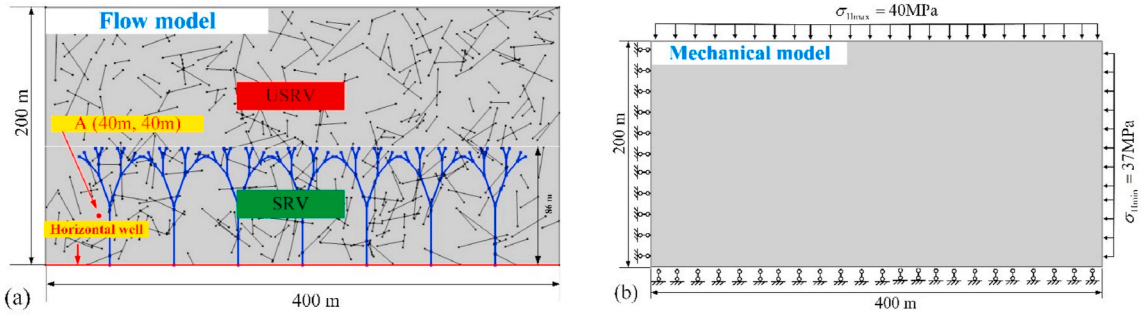

Fig. 13. Schematic of physical geometry and boundary conditions used in modelling.

the prototype model in Section 4. The model includes the NF networks and fractal tree-like HF networks. The base case comprises a total of 400 NFs, with a mean length of 40m and variance of 100 m^2. The HFN consists of seven primary fractures, with a branch level of four and a bifurcation ratio of 40°. The spacing between the adjacent HFs is 50m. The zone below the multi-level HFs is the SRV with the zone above the HFs as USRV. The modelling parameters are listed in Table 2. All other parameters are identical to the parameters used in the field verification.

5.1. Impact of OM heterogeneity on apparent permeability and flow regime

To illustrate the impacts of OM heterogeneity on apparent permeability and flow regime, various values of fractal dimension are adopted (D_{ho} = 1.1, 1.2, 1.3, 1.4 and 1.5) for simulation and sensitivity analyses. Point A (40m, 40m) is selected as the representative point to demonstrate the results, as indicated in Fig. 13 (a). As shown in Fig. 14 (a), the apparent permeability of the OM increases with a decrease in pore pressure – as the desorption-induced pore shrinkage counteracts the increased effective stress. In addition, the growth of Knudsen diffusion and surface diffusion-contributed permeability also enhances the apparent permeability. According to Fig. 14 (b), the relative contribution of viscous flow to gas recovery decreases as the reservoir pressure drops. When the pressure is reduced to 10 MPa, the contribution of viscous flow to total recovery falls below 50 %. An increase in fractal dimensions of the OM PSD corresponds to an increasingly lower contribution ratio (to total recovery) due to the increasing number of small pores and hence a decreased average pore radius. By contrast, Fig. 14 (c) demonstrates that the contribution ratio of Knudsen diffusion increases with a decline in pore pressure, with this proportion increasing with an increase in the fractal dimensions of the OM PSD. As presented in Fig. 14 (d), surface diffusion exerts only a marginal impact on apparent permeability, accounting for less than a 5 % change even with the increase in pore pressure. Moreover, higher fractal dimensions of the OM PSD result in a larger contribution of Knudsen diffusion to recovery, due to the decreasing average pore radius. Therefore, it can be concluded that when gas pressure declines, Knudsen diffusion begins to dominate the apparent permeability represented by the shale nanopores. The larger fractal dimensions of the OM PSD indicates higher contribution ratios from Knudsen diffusion and lower contribution ratios from viscous flow, - again, due to the decrease in average pore radius.

Table 2
Modelling parameters used in sensitivity analyses.

Parameters	Value	Unit
Fractal dimension of PSD in OM	1.1–1.5	
Fractal dimension of PSD in IOM	1.1–1.5	
Compressibility of IOM	4.5×10^{-10}	Pa^{-1}
Minimum pore size of IOM	1–5	nm
Maximum pore size of IOM	100–500	nm
Initial NF permeability	1.5mD	
NF width	0.0005	m
Number of NFs	200–500	
HF width	0.003	m
Number of primary HFs	14	
Bifurcate angle	40–100°	°
Branching ratio	2	
Branching level	1–4	
HF spacing	50	m
Initial HF permeability	100	mD
Half-length of primary HF	45	m

5.2. Stress sensitivity of shale reservoir

5.2.1. Impacts of compressibility on permeability evolution

Compressibility of shale matrix and fracture network exhibits a pivotal role in shale deformation, thereby affecting shale permeability and gas production rate. Experiments demonstrate that rock fracture compressibility is far larger than that of rock matrix (Zhang et al., 2019). In practical situation, due to the proppant in hydraulic fractures, the compressibility of hydraulic fracture is smaller than that of natural fracture network (Tan et al., 2019). To investigate the impacts of compressibility of OM (c_k), compressibility of IOM (c_m), compressibility of NFN (c_{nf}) and compressibility of HFN (c_{hf}) on permeability evolution, various values have been adopted to conduct sensitivity analysis, as shown in Fig. 15 (a)-(d). For the OM system, when c_k increases from 7×10^{-10} Pa^{-1} to 1.6×10^{-9}, the permeability ratio drops from 1.28 to 1.26 when the production time is 30 years, indicating that higher c_k results in decrease of OM permeability. Moreover, as displayed in Fig. 15 (b), when c_m increases from 5×10^{-11} Pa^{-1} to 3×10^{-10} Pa^{-1}, the IOM permeability ratio decreases from 0.886 to 0.877. By contrast, permeability ratios of NFN and HFN show 15 % and 10 % decline whenc_{nf} is raised from 3×10^{-9} Pa^{-1} to 9×10^{-9} Pa^{-1} and c_{hf} is raised from 2×10^{-9} Pa^{-1} to 8×10^{-9} Pa^{-1}. It can be concluded that increase of compressibility results in the decrease of permeability because shale is more easily compressed when shale is subjected to effective stress. All the four hierarchical systems (OM, IOM, NFNs and HFNs) are sensitive to the variation of compressibility. Compared with the shale matrix consisting of OM and IOM, HFNs and HFNs are more sensitive to the variation of compressibility. It should be noted that the compressibility of shale matrix is affected by multiple factors like pore structures and mineral compositions. Particularly, those clay-rich shale samples have larger IOM compressibility than those samples that contain a higher percentage of quartz and feldspars (Josh et al., 2012; Kumar et al., 2012). Therefore, the permeability ratio of IOM can experience larger fluctuation when compressibility varies.

5.2.2. Evolution of shale deformation

Gas depletion from shale reservoir increases effective stress and compaction of shale solid skeleton. However, gas desorption can induce shale matrix shrinkage. These two competitive effects decide the shale deformation jointly. The evolution of shale deformation can be illustrated through the variation of time-dependent volumetric strain. According to Eq. (1), volumetric strain is comprised of three components,

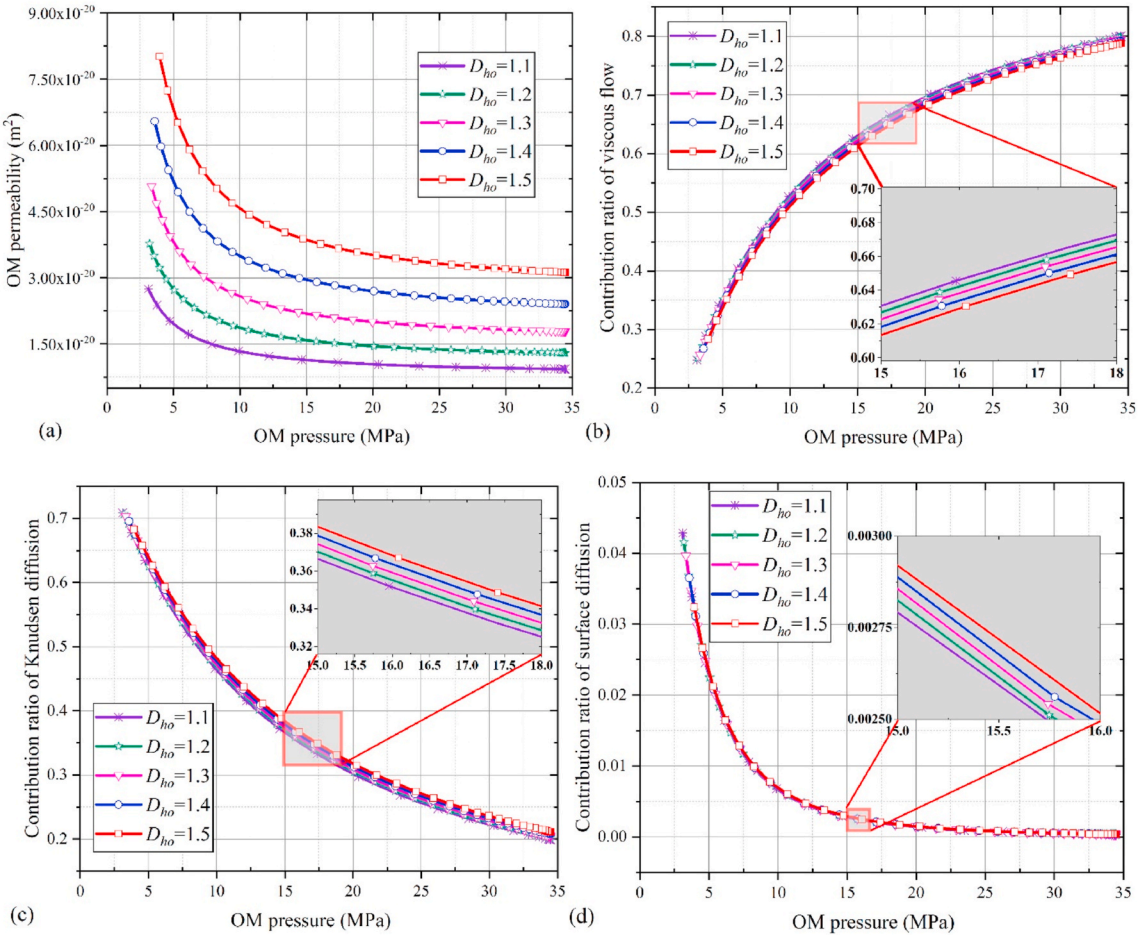

Fig. 14. Impacts of fractal dimensions of OM PSD on gas flow.

which are OM pressure-induced strain (ε_v^k), IOM pressure-induced strain (ε_v^m) and desorption-induced shrinkage strain (ε_v^s), respectively. These strains are expressed in the following equations (Lu et al., 2021):

$$\varepsilon_v^k = \frac{\alpha^k \Delta p_k}{K} \tag{19}$$

$$\varepsilon_v^m = \frac{\alpha^m \Delta p}{K} \tag{20}$$

$$\varepsilon_v^s = \frac{\Delta \sigma_s}{K} \tag{21}$$

As shown in Fig. 16, all the three attributes of volumetric strain (ε_v^k, ε_v^m and ε_v^s) increase with production time. When the production time is 30 years, ε_v^k, ε_v^m and ε_v^s are 9×10^{-5}, 4.5×10^{-4} and 1.29×10^{-3} respectively, which indicates that the IOM pressure-induced strain plays the most important role in shale deformation because of the larger pressure drop and effective stress coefficient. By contrast, the desorption-induced strain plays a marginal role in shale deformation. Fig. 17 presents the spatial distribution of the total volumetric strain at various production times. It can be seen that, at the beginning of shale production, the volumetric strain around the HFNs spikes, with the largest difference between the HFNs and the further side of the reservoir. With the increase of production time and propagation of pressure drawdown, the volumetric strain gap between the near-well region and further side gradually decreased. The presence of the fracture network results in the local surge of volumetric strain and heterogeneous distribution of shale deformation.

5.3. Impact of OM and IOM heterogeneity on gas production

The influence of the fractal dimension and pore diameter on gas production for the OM and IOM are now investigated. For the OM, five sets of fractal dimensions (D_{ho} = 1.1, 1.2, 1.3, 1.4 and 1.5) and minimum pore diameters (h_{minio} = 1.0, 1.5, 2.0, 2.5 and 3 nm) are selected to perform sensitivity and parametric analyses. Fig. 18 (a) and Fig. 18 (b) present the cumulative gas production levels from the OM for various fractal dimensions and minimum pore diameters. When the fractal dimension increases from 1.1 to 1.5 (the minimum pore diameter is fixed as 1 nm), the cumulative gas production increases from 6.5×10^7 m^3 to 7.4×10^7 m^3 over a production period of 30 years - corresponding to a 12 % growth. When the fractal dimension (D_{ho} = 1.3) and the corresponding porosity (φ_k = 0.065) remain constant, the variation in minimum pore diameter significantly affects the average pore diameter. As shown in Fig. 18 (b), when the minimum pore diameter of the OM is 1 nm, the cumulative gas production reaches 6.95×10^7 m^3. By contrast, when the minimum pore diameter increases to 3 nm, cumulative gas production increases by 8.9 % to reach 7.63×10^7 m^3. The fractal dimension of the OM PSD correlates to its porosity and pore diameter. A larger fractal dimension indicates a broader spectrum of PSD and larger porosity. When the maximum and minimum pore diameter are both fixed a larger fractal dimension contributes to more small pores. Consideration of the PSD in production forecasting is necessary to improve the accuracy of the prediction.

For the IOM, five sets of fractal dimensions (D_{hi} = 1.1, 1.2, 1.3, 1.4 and 1.5) are employed to study the corresponding influences on gas production. Pore sizes in the IOM span a range of several orders-of-magnitude and are observed to typically be larger than that of OM

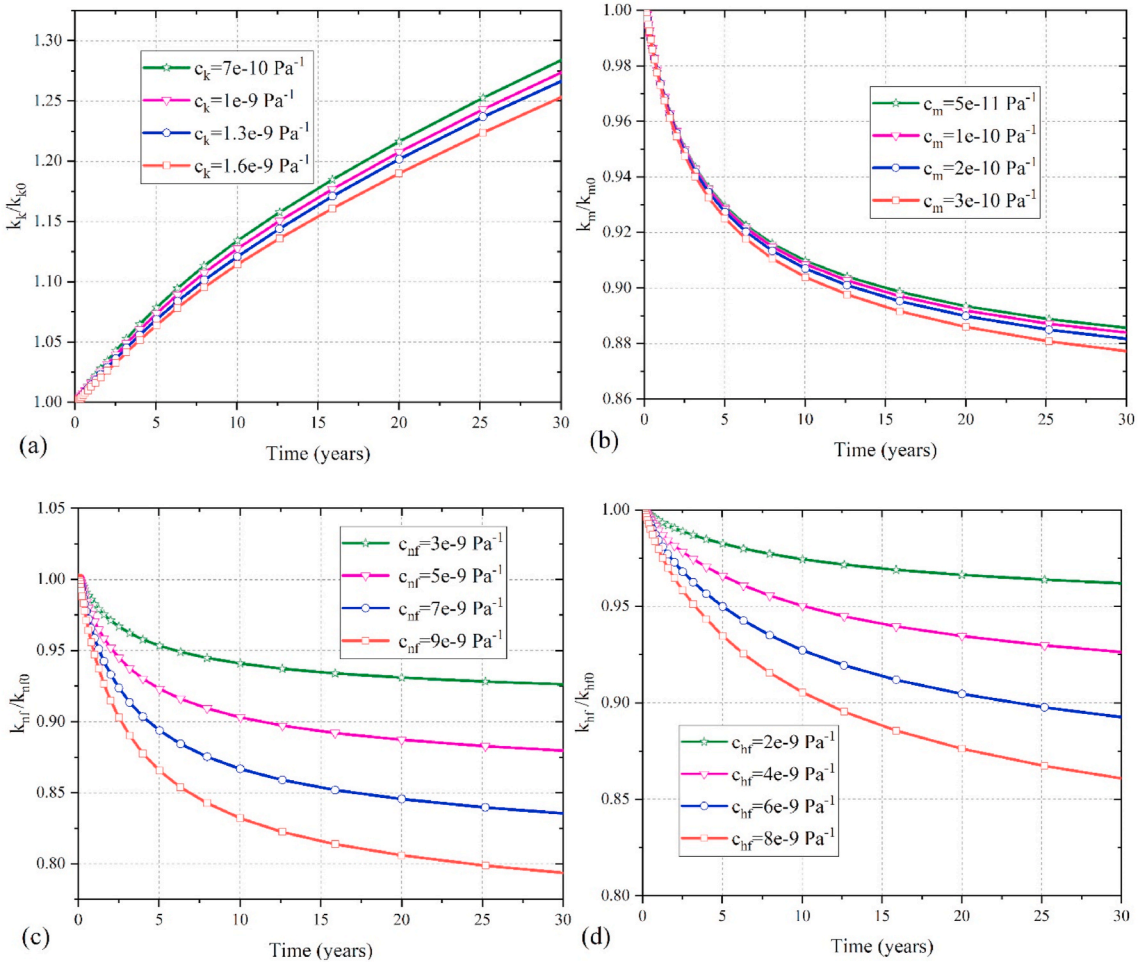

Fig. 15. Impacts of compressibility on the permeability evolution of hierarchical systems: (a) OM; (b) IOM; (c) Natural fracture; (d) Hydraulic fracture.

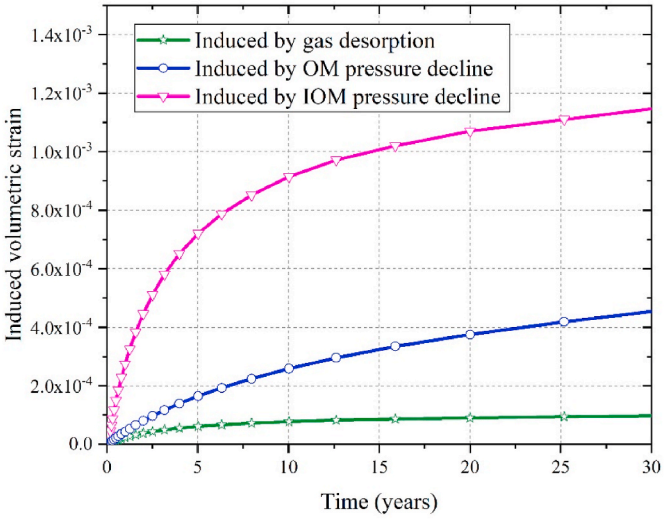

Fig. 16. Evolutions of induced volumetric strains for different factors.

(Wang et al., 2019). Therefore, minimum pore diameters ranging from 1 nm to 5 nm are considered in the simulation. As shown in Fig. 19 (a), a larger fractal dimension correlates to higher levels of cumulative gas production. When the fractal dimension of the IOM PSD increases from 1.1 to 1.5, the cumulative gas production increases from 5.1 $\times$ 10^7 m^3 to 9.1 $\times$ 10^7 m^3, displaying a significant growth of 78 %. At the same time, when the maximum pore diameter of the IOM increases from the base case to 500 nm, the cumulative gas production increases by 33 %, as shown in Fig. 19 (b). Compared to the experimental observations for the OM, the fractal dimension and minimum pore diameters of the IOM exert a greater impact on gas production from the IOM than the OM. Thus, one can conclude that the major control on gas recovery is the permeability of the IOM. If the fractal dimension of the IOM PSD is not considered, a significant underestimate in the final gas production level may result.

5.4. *Impact of NFs on gas production*

The stochastic distribution of NFs is one of the prominent heterogeneities evident at the macroscale. We investigate the impact of NF density (NF number) on gas production based on four NFN groups (200, 300, 400 and 500 natural fractures). Fig. 20 presents the IOM pressure distribution for simulations with the four groups over a production period of 30 years. When the number of NFs increases, the range of matrix pressures narrows - suggesting that higher fracture densities facilitate accelerated gas depletion. As shown in Fig. 21 (a), when the number of NFs increases from 200 to 500, the cumulative gas production increases from 6.4 $\times$ 10^7 m^3 to 7.3 $\times$ 10^7 m^3 - an ~12 % increment. We may also compare the significance of NFNs to the evolution of IOM porosity, as shown in Fig. 21 (b). It can be noted that the IOM porosity declines with gas depletion because of the decreased reservoir pressure and increased effective stress. When the production time is 30 years, the IOM porosity decreases from 0.4 to 0.395. Moreover, higher fracture densities increase the gas production rate, which results in more rapid

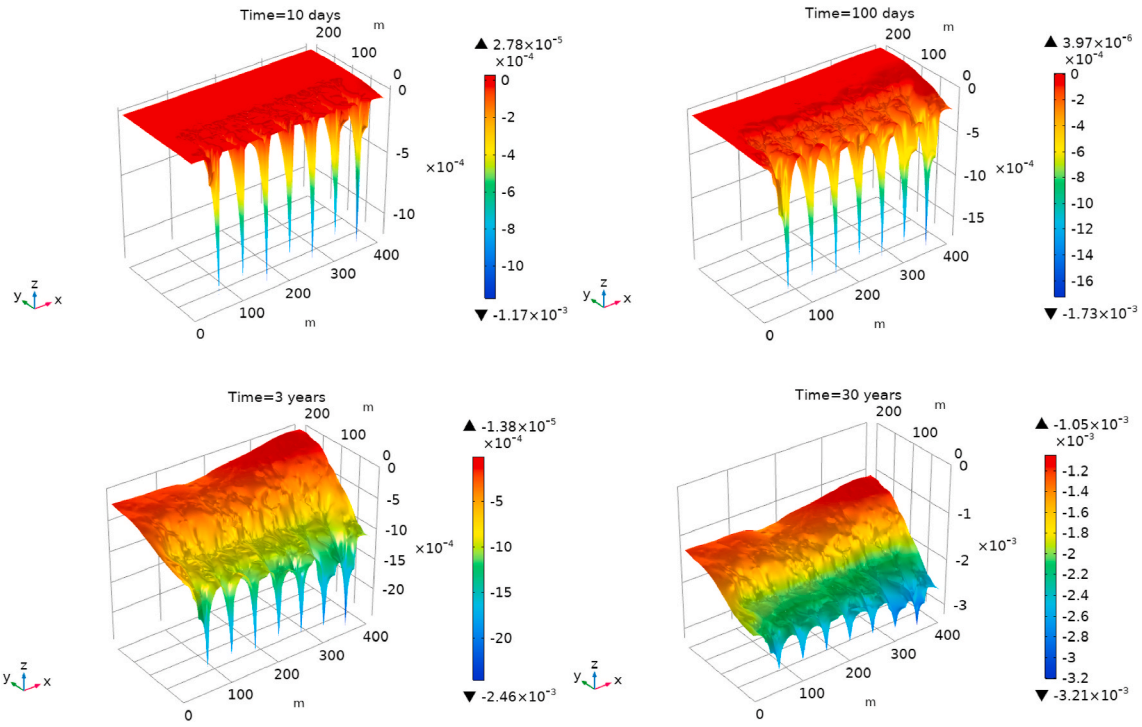

Fig. 17. Spatial distribution of volumetric strain at different production times.

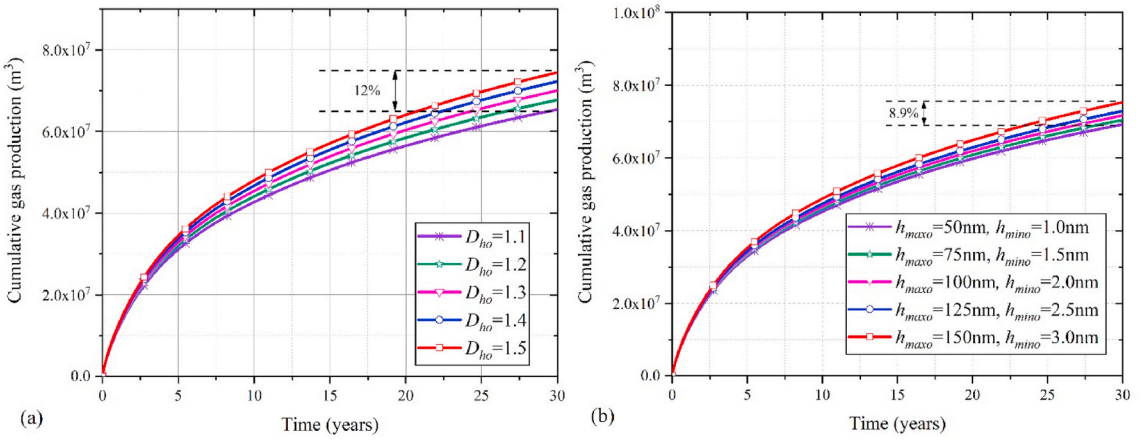

Fig. 18. Impacts of PSD and minimum pore diameter of OM on cumulative gas production.

decrease of inorganic matrix porosity.

5.5. Impact of HF distribution on gas production

The presence of artificial hydraulic fracture networks is another hierarchical structural heterogeneity at macroscale that potentially affects gas production. The primary HF and the induced secondary fractures are characterized as a branched dendritic network. The primary controlling factors are the branching levels (1, 2, 3 and 4 in this study) and bifurcation angles (40°, 60°, 80° and 100° in this study). It should be noted that the branching levels and the bifurcation ratio of the generated HFs are concurrently controlled by the orientation of principal stresses and properties of the reservoir (Hossain et al., 2000). This study uses a fractal ratio of two, which implies that fracture lengths and diameter ratios decrease progressively in steps of one-half. Fig. 22 presents the matrix pressure distributions for the four groups with varying fracture levels over a production time of 120 days. Fig. 23 (a) demonstrates that cumulative gas production increase with an increase in fracture level. This can be attributed to the fact that multi-level HFs enlarge the SRV and facilitate gas desorption and outflows from that reservoir. When the number of HFs increases from one to four, the cumulative gas production increases from 5.4 × 10^7 m^3 to 6.9 × 10^7 m^3, corresponding to an increment of 29 %.

Bifurcation angles define the propagation direction of the HFs. The surface map of IOM pressure over a production period of 120 days is presented in Fig. 24. The impacts of the bifurcation angle on gas production are shown in Fig. 23 (b). When the angle increases from 40° to 100°, the cumulative gas production decreases. This phenomenon occurs mainly due to the decrease in the size of the SRV in the vertical direction. More than that, when the bifurcation ratio is larger than 40°, secondary fractures between adjacent HFNs become interconnected, resulting in strong fracture interference and thereby decreasing the gas productivity (Yu et al., 2014). A detailed evaluation of the impacts of fracture interference on gas productivity warrants further investigation.

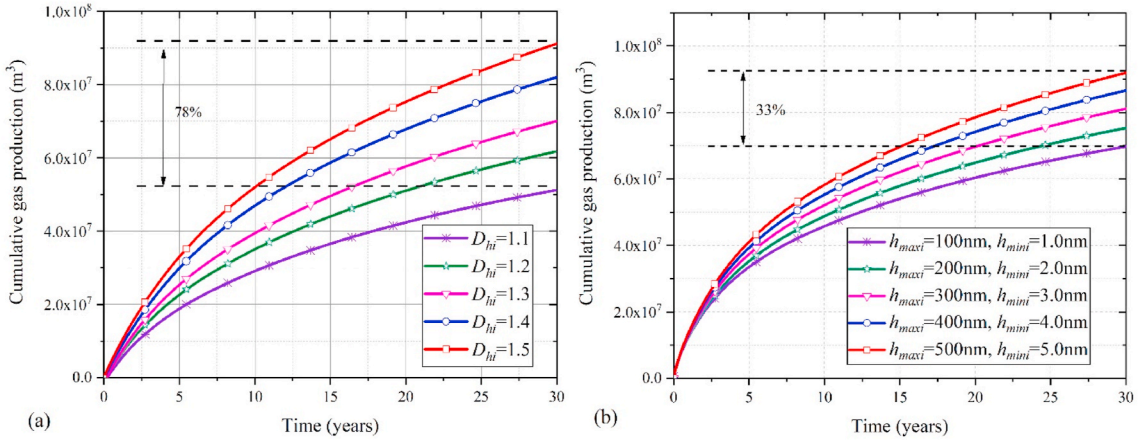

Fig. 19. Impacts of the fractal dimension of PSD and minimum pore diameters in IOM on gas production.

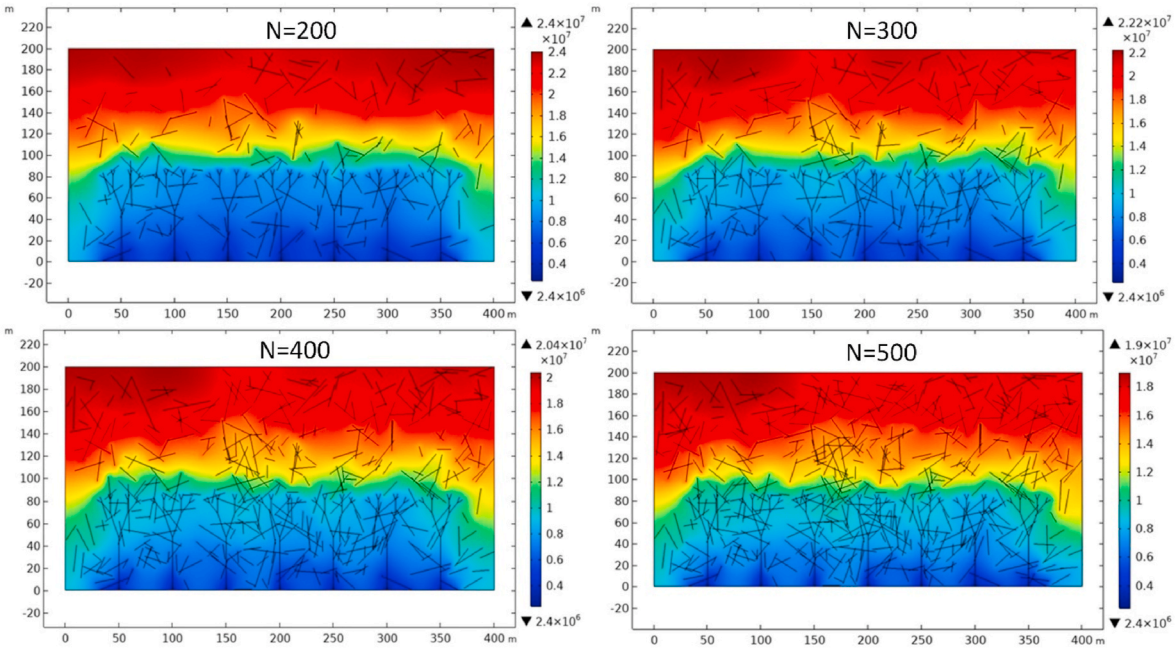

Fig. 20. IOM pressure distribution for various number of NFs.

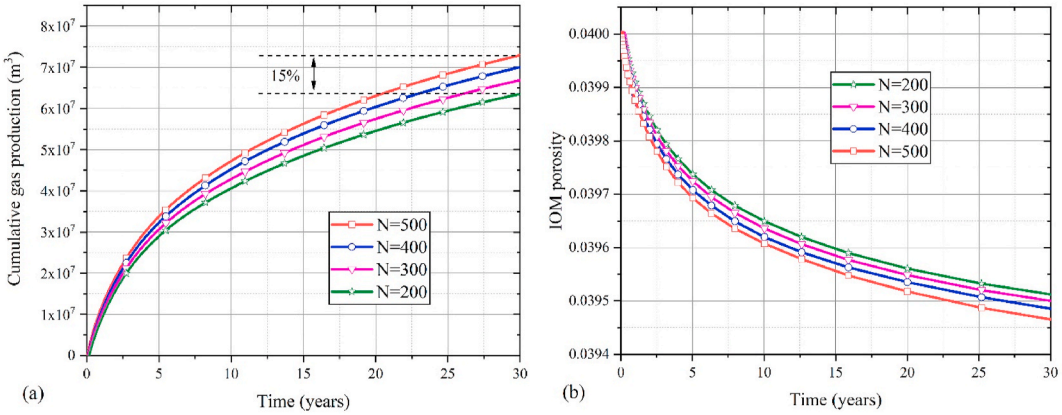

Fig. 21. Impacts of fracture density of NFs on cumulative gas production.

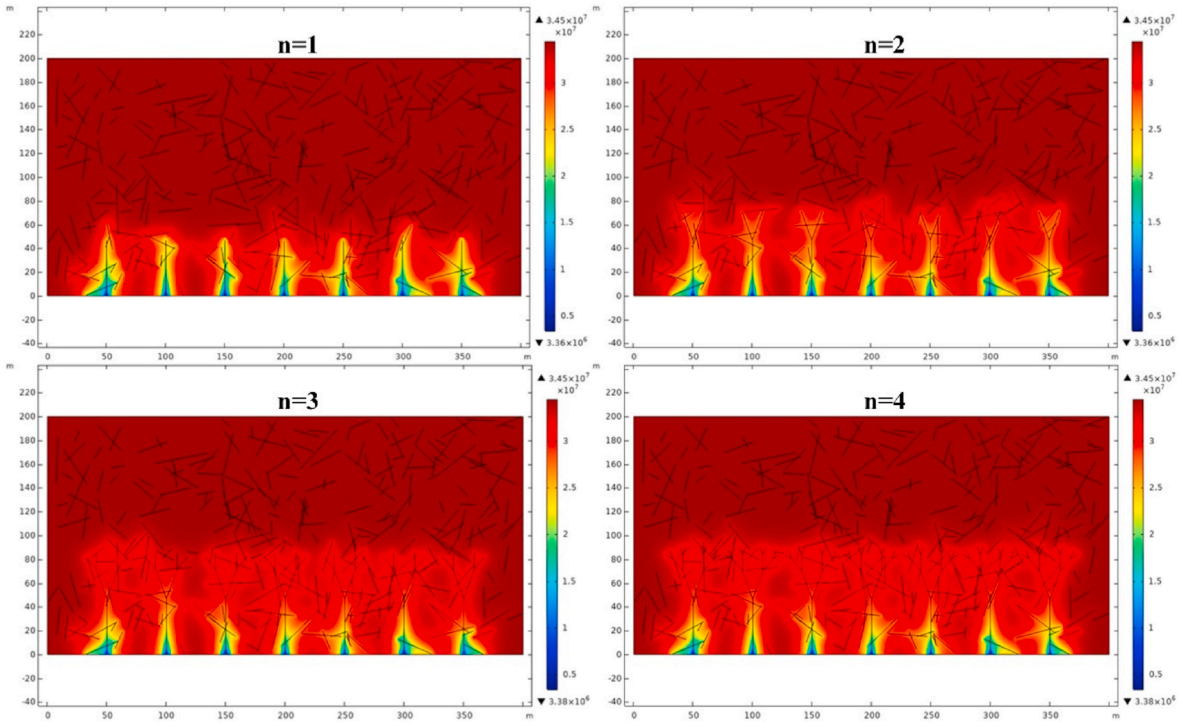

Fig. 22. Surface maps of matrix pressure for different densities of HFs.

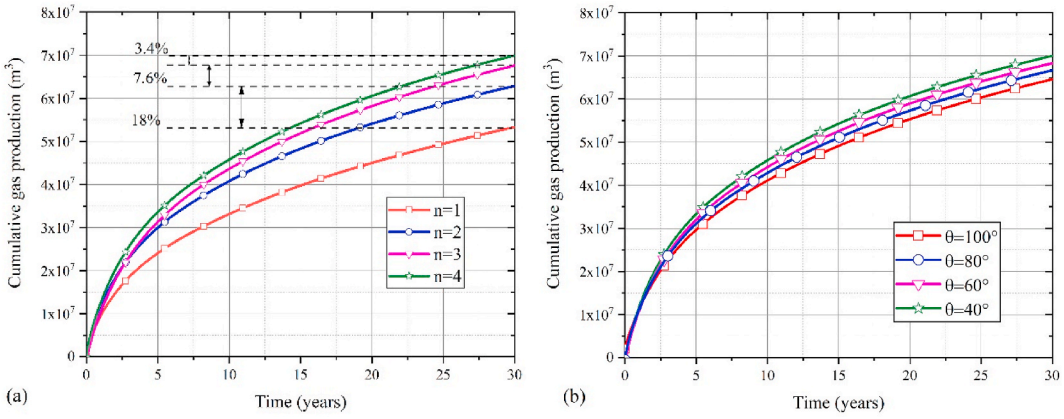

Fig. 23. Impacts of various HF schemes on gas production.

6. Conclusions

A fully coupled model of gas flow and shale deformation is developed to quantify the impacts of multiscale heterogeneities on gas production. A mechanical equilibrium equation is applied to the whole reservoir system. The matrix permeability is dependent on the effective stress and matrix swelling while the fracture permeability is pressure-dependent. Heterogeneous pore size distributions within both organic and inorganic matter are characterized at the microscale using a fractal approach, while the fracture networks at the macroscale are represented explicitly. Modelling results demonstrate that heterogeneities at all scales are important but their roles differ significantly during gas production:

(1) For the organic matter (OM), higher fractal dimensions denote a larger porosity with more smaller pores. Model results show that the relative contribution of overall production due to surface diffusion and Knudsen diffusion increases with the fractal dimension of the organic matter when the gas pressure is low. However, this heterogeneous impact decreases when the gas pressure is high.

(2) The inorganic matter (IOM) provides both storage sites for gas and conduits for its flow once it is released from the organic matter. Model results show that the fractal dimension and range between maximum and minimum pore sizes affect gas production, and that variations in maximum and minimum pore diameter can cause significant fluctuations in permeability and production rate.

(3) Natural fractures act as primary passages for gas released from both the organic and inorganic matter. Model results show that both the natural fracture density and the evolution of individual fracture permeability affect gas production rate, and that their impact on gas production is significant throughout the entire production process.

(4) Hydraulic fractures collect gas released from all sources in series (organic and inorganic matters, and natural fractures) and

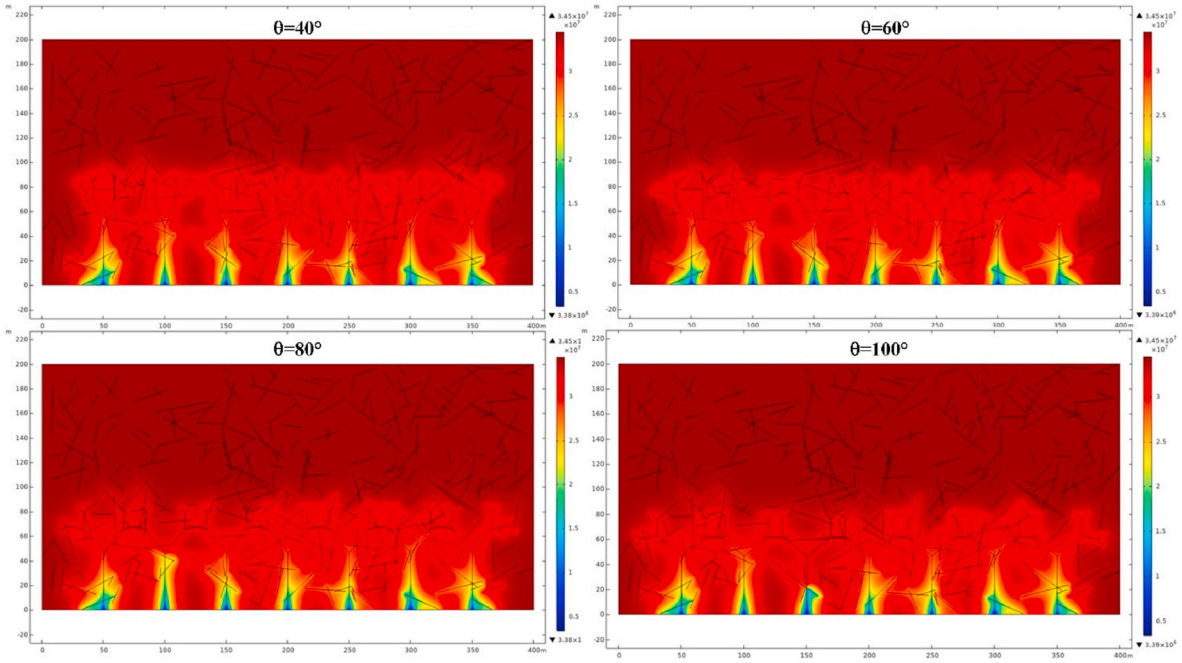

Fig. 24. Surface maps of matrix pressure for different HF bifurcation angles.

transport it to the production well. Model results show that the fractal branched dendritic networks are much more effective in capturing and transmitting gas than unbranched straight fractures, and that the role of the number of hydraulic fractures is also controlled by the gas supplied from the organic matter, inorganic matter, and natural fractures.

Declaration of competing interest

The authors declare that they have no known competing financial interests or personal relationships that could have appeared to influence the work reported in this paper.

Acknowledgements

This work is supported by the Australian Research Council under Grant DP200101293. The first author is supported by the UWA-China Joint Scholarships (grant number: 201706430057).

Appendix A. Derivation of the apparent permeability of OM

The pore size in the shale matrix varies from nanometres to micrometres, which complicates the gas flow mechanisms in the tortuous flow channels. In this study, the pore size distribution (PSD) in shale is assumed following fractal theory, the cumulative number of pores N is defined as (Yu and Li, 2001) :

$$N(H \geq h) = \left(\frac{h_{\max}}{h}\right)^{D_h} \tag{A1}$$

where the $h_{\max}$ is the maximum pore diameter, D_h is the fractal dimension of PSD. The infinitesimal increment of pore number is expressed as:

$$-dN = D_h (h_{\max})^{D_h} h^{-(D_h+1)} dh \tag{A2}$$

The area of pore space for the cross-section can be determined by integrating all of the pores:

$$A_p = -\int_{h_{\min}}^{h_{\max}} \frac{1}{4}\pi h^2 dN = \int_{h_{\min}}^{h_{\max}} \frac{1}{4}\pi h^2 D_h h_{\max}^{D_h} h^{-(D_h+1)} dh = \frac{\pi D_h h_{\max}^2}{4(2-D_h)}\left[1-\left(\frac{h_{\min}}{h_{\max}}\right)^{2-D_h}\right] \tag{A3}$$

where the $h_{\min}$ is the minimum pore diameter, the cross-section area of the REV is derived as:

$$A = \frac{A_p}{\varphi} = \frac{\pi D_h h_{\max}^2}{4\varphi(2-D_h)}(1-\varphi) \tag{A4}$$

The tortuous flow length of the corresponding pore diameter h is given as (Yu and Li, 2001) :

$$L_T = L_0^{D_T} h^{1-D_T} \tag{A5}$$

where the L_T is the real flow length, L_0 is the length of the REV, $D_T$is the fractal dimension of tortuosity. The tortuosity of the pores is defined as the ratio of true flow length and straight flow length:

$$\tau = \frac{L_T}{L_0} = \left(\frac{L_0}{h}\right)^{D_T - 1} \tag{A6}$$

The total gas flux through the shale matrix is typically a combination of viscous fraction and diffusion fraction. The apparent permeability of a single nanopore is expressed as (Cao et al., 2016b):

$$k = k_v + k_n + k_s = \frac{\varphi_k}{\tau}\frac{h^2}{32} + \frac{\varphi_k}{\tau}\frac{\mu h}{3p_k}\sqrt{\frac{8RT}{\pi M_g}} + \frac{\mu D_s P_L C_{us} RT}{(p_k + P_L)^2 p_k} \tag{A7}$$

where φ_k is the kerogen porosity, h is the pore diameter, D_s is the surface diffusion coefficient, C_{us} is the maximum adsorbed gas concentration in unit volume of kerogen, which is defined as (Cao et al., 2016a):

$$C_{us} = \rho_{ga}\rho_s\frac{V_L}{M} \tag{A8}$$

Combined A (6) and A (7), the total molar flux considering the viscous flow, Knudsen diffusion and surface diffusion in a nanopore can be written as:

$$J_t = J_v + J_n + J_s = \frac{\varphi_k \pi h^4}{128\mu}\frac{\Delta p_k}{L_T} + \sqrt{\frac{2\pi RT}{M_g}}\frac{\varphi_k h^3}{6p_k}\frac{\Delta p_k}{L_T} + \frac{D_s P_L C_{us} RT}{(p_k + P_L)^2 p_k}\frac{\pi h^2}{4}\frac{\Delta p_k}{L_T} \tag{A9}$$

where the L_T is the tortuous flow length. Since the pores are fractally distributed in OM, the total gas flux through the OM can be integrated as:

$$Q = Q_v + Q_n + Q_s = \int_{h_{\min}}^{h_{\max}} (J_v + J_n + J_s)\, dN \tag{A10}$$

Substituting Eq. (A9) into (A10), the total molar flux of each flow regime can be obtained as:

$$\begin{cases} Q_v = \dfrac{\pi}{128\mu}\dfrac{\varphi_k D_{ho} h_{\max o}^{3+D_{To}}}{3 + D_{To} - D_{ho}}\dfrac{\Delta p}{L_0^{D_T}}\left[1 - \left(\dfrac{h_{\min}}{h_{\max}}\right)^{3+D_{To}-D_{ho}}\right] \\ Q_n = \sqrt{\dfrac{2\pi RT}{M_g}}\dfrac{1}{6p_k}\dfrac{\varphi_k D_{ho} h_{\max o}^{2+D_{To}}}{2 + D_{To} - D_{ho}}\dfrac{\Delta p}{L_0^{D_{To}}}\left[1 - \left(\dfrac{h_{\min o}}{h_{\max o}}\right)^{2+D_{To}-D_{ho}}\right] \\ Q_s = \dfrac{\pi D_s P_L C_{us} RT}{(p_k + P_L)^2 p_k}\dfrac{\varphi_k D_{ho} h_{\max o}^{1+D_{To}}}{2 + D_{To} - D_{ho}}\dfrac{\Delta p}{L_0^{D_{To}}}\left[1 - \left(\dfrac{h_{\min o}}{h_{\max o}}\right)^{1+D_{To}-D_{ho}}\right] \end{cases} \tag{A11}$$

Combined with Eq. (A11) and Darcy law $Q = Ak\Delta p/\mu/L_0$, the apparent permeability of each flow regime is expressed as:

$$\begin{cases} k_v = \dfrac{\pi}{128}\dfrac{\varphi_k D_{ho}}{3 + D_{To} - D_{ho}}\dfrac{h_{maxo}^{3+D_{To}}}{L_0^{D_{To}+1}} \\ k_n = \sqrt{\dfrac{2\pi RT}{M_g}}\dfrac{\varphi_k \mu D_{ho}}{(2 + D_{To} - D_{ho})}\dfrac{h_{\max o}^{2+D_{To}}}{6p_k L_0^{D_{To}+1}} \\ k_s = \dfrac{\pi D_s P_L C_{us} RT}{(p_k + P_L)^2 p_k}\dfrac{\mu D_{ho}}{(2 + D_{To} - D_{ho})}\dfrac{h_{\max o}^{1+D_{To}}}{L_0^{D_{To}+1}} \end{cases} \tag{A12}$$

Then, it yields the fractal-based apparent permeability for shale OM:

$$\begin{aligned} k_k = \frac{\pi}{128}\frac{D_{ho}}{3 + D_{To} - D_{ho}}\frac{h_{maxo}^{3+D_{To}}}{L_0^{D_{To}+1}} + \sqrt{\frac{2\pi RT}{M_g}}\frac{\mu D_{ho}}{(2 + D_{To} - D_{ho})}\frac{h_{\max o}^{2+D_{To}}}{6p_k L_0^{D_{To}+1}} \\ + \frac{\pi D_s P_L C_{us} RT}{(p_k + P_L)^2 p_k}\frac{\mu D_{ho}}{(2 + D_{To} - D_{ho})}\frac{h_{\max o}^{1+D_{To}}}{L_0^{D_{To}+1}} \end{aligned} \tag{A13}$$

Credit author statement

Jianwei Tian: Methodology, Investigation, Writing – original draft Preparation. Jishan Liu: Supervision, Methodology, Writing-Reviewing and Editing. Derek Elsworth: Supervision, Writing-Reviewing and Editing. Yee-Kwong Leong: Supervision, Conceptualization. Wai Li: Methodology, Conceptualization. Jie Zeng: Methodology, Conceptualization.

References

Akkutlu, I.Y., Efendiev, Y., Vasilyeva, M., Wang, Y., 2017. Multiscale model reduction for shale gas transport in a coupled discrete fracture and dual-continuum porous media. J. Nat. Gas Sci. Eng. 48, 65–76.

Akkutlu, I.Y., Fathi, E., 2012. Multiscale gas transport in shales with local kerogen heterogeneities. SPE J. 17 (4), 1,002-1,011.

Ambrose, R.J., Hartman, R.C., Diaz Campos, M., Akkutlu, I.Y., Sondergeld, C., 2010. New Pore-Scale Considerations for Shale Gas in Place Calculations, SPE Unconventional Gas Conference. Society of Petroleum Engineers.

Bai, M., Elsworth, D., 2000. Coupled Processes in Subsurface Deformation, Flow, and Transport. American Society of Civil Engineers.

Bai, M., Elsworth, D., Roegiers, J.C., 1993. Multiporosity/multipermeability approach to the simulation of naturally fractured reservoirs. Water Resour. Res. 29 (6), 1621–1633.

Barenblatt, G.I., Zheltov, I.P., Kochina, I.N., 1960. Basic concepts in the theory of seepage of homogeneous liquids in fissured rocks [strata]. J. Appl. Math. Mech. 24 (5), 1286–1303.

Barton, C.M., 1978. Analysis of joint traces. In: 19th US Symposium on Rock Mechanics (USRMS). American Rock Mechanics Association.

Blanton, T.L., 1986. Propagation of hydraulically and dynamically induced fractures in naturally fractured reservoirs. In: SPE Unconventional Gas Technology Symposium. Society of Petroleum Engineers.

Bridges, M.C., 1975. Presentation of fracture data for rock mechanics. In: Second Australia-New Zealand Conference on Geomechanics. Institution of Engineers, Australia, p. 144.

Bu, H., Ju, Y., Tan, J., Wang, G., Li, X., 2015. Fractal characteristics of pores in non-marine shales from the Huainan coalfield, eastern China. J. Nat. Gas Sci. Eng. 24, 166–177.

Cai, J., Lin, D., Singh, H., Wei, W., Zhou, S., 2018. Shale gas transport model in 3D fractal porous media with variable pore sizes. Mar. Petrol. Geol. 98, 437–447.

Cao, P., Liu, J., Leong, Y.-K., 2016a. Combined impact of flow regimes and effective stress on the evolution of shale apparent permeability. Journal of Unconventional Oil and Gas Resources 14, 32–43.

Cao, P., Liu, J., Leong, Y.-K., 2016b. A fully coupled multiscale shale deformation-gas transport model for the evaluation of shale gas extraction. Fuel 178, 103–117.

Chen, J., et al., 2016. Experimental investigation of the characteristics of organic matter pores in Chang 7 member lacustrine shale from the Ordos Basin due to organic matter evolution induced by hydrous pyrolysis. J. Nat. Gas Sci. Eng. 35, 412–424.

Chen, T., Feng, X.-T., Cui, G., Tan, Y., Pan, Z., 2019. Experimental study of permeability change of organic-rich gas shales under high effective stress. J. Nat. Gas Sci. Eng. 64, 1–14.

Chen, Y., Nagaya, Y., Ishida, T., 2015. Observations of fractures induced by hydraulic fracturing in anisotropic granite. Rock Mech. Rock Eng. 48 (4), 1455–1461.

Cui, G., Liu, J., Wei, M., Shi, R., Elsworth, D., 2018. Why shale permeability changes under variable effective stresses: new insights. Fuel 213, 55–71.

Cui, X., Bustin, R.M., 2005. Volumetric strain associated with methane desorption and its impact on coalbed gas production from deep coal seams. AAPG Bull. 89 (9), 1181–1202.

Fan, D., Ettehadtavakkol, A., 2017. Semi-analytical modeling of shale gas flow through fractal induced fracture networks with microseismic data. Fuel 193, 444–459.

Gale, J.F.W., Laubach, S.E., Olson, J.E., Eichhubl, P., Fall, A., 2014. Natural fractures in shale: a review and new observationsNatural fractures in shale: a review and new observations. AAPG Bull. 98 (11), 2165–2216.

Geng, L., et al., 2018. A fractal production prediction model for shale gas reservoirs. J. Nat. Gas Sci. Eng. 55, 354–367.

Guo, X., Shen, Y., He, S., 2015. Quantitative pore characterization and the relationship between pore distributions and organic matter in shale based on Nano-CT image analysis: a case study for a lacustrine shale reservoir in the Triassic Chang 7 member, Ordos Basin, China. J. Nat. Gas Sci. Eng. 27, 1630–1640.

Hossain, M.M., Rahman, M.K., Rahman, S.S., 2000. Hydraulic fracture initiation and propagation: roles of wellbore trajectory, perforation and stress regimes. J. Petrol. Sci. Eng. 27 (3–4), 129–149.

Jiang, J., Younis, R.M., 2015. A multimechanistic multicontinuum model for simulating shale gas reservoir with complex fractured system. Fuel 161, 333–344.

Josh, M., et al., 2012. Laboratory characterisation of shale properties. J. Petrol. Sci. Eng. 88, 107–124.

Kazemi, H., 1969. Pressure transient analysis of naturally fractured reservoirs with uniform fracture distribution. Soc. Petrol. Eng. J. 9 (4), 451–462.

Kazemi, H., Gilman, J.R., Elsharkawy, A.M., 1992. Analytical and numerical solution of oil recovery from fractured reservoirs with empirical transfer functions (includes associated papers 25528 and 25818). SPE Reservoir Eng. 7 (2), 219–227.

Kumar, V., Sondergeld, C.H., Rai, C.S., 2012. Nano to macro mechanical characterization of shale, SPE annual technical conference and exhibition. OnePetro, SPE-159804-MS. SPE-159804-MS.

Lan, Y., et al., 2019. A review of microscopic seepage mechanism for shale gas extracted by supercritical CO2 flooding. Fuel 238, 412–424. ISRM-YSRM-2019-063.

Li, A., et al., 2016. Investigation of pore structure and fractal characteristics of organic-rich shale reservoirs: a case study of Lower Cambrian Qiongzhusi formation in Malong block of eastern Yunnan Province, South China. Mar. Petrol. Geol. 70, 46–57.

Li, W., et al., 2020. A fully coupled multidomain and multiphysics model for evaluation of shale gas extraction. Fuel 278, 118214.

Li, W., Liu, J., Zeng, J., Leong, Y.K., Elsworth, D., 2019. A fully coupled multidomain and multiphysics model for shale gas production, 5th ISRM young scholars' symposium on rock mechanics and international symposium on rock engineering for innovative future. International Society for Rock Mechanics and Rock Engineering.

Lu, Y., Wei, S., Xia, Y., Jin, Y., 2021. Modeling of geomechanics and fluid flow in fractured shale reservoirs with deformable multi-continuum matrix. J. Petrol. Sci. Eng. 196, 107576.

Manzocchi, T., 2002. The connectivity of two-dimensional networks of spatially correlated fractures. Water Resour. Res. 38 (9), 1-1-1-20.

Mi, L., Jiang, H., Li, J., Li, T., Tian, Y., 2014. The investigation of fracture aperture effect on shale gas transport using discrete fracture model. J. Nat. Gas Sci. Eng. 21, 631–635.

Nandlal, K., Weijermars, R., 2019. Drained rock volume around hydraulic fractures in porous media: planar fractures versus fractal networks. Petrol. Sci. 16 (5), 1064–1085.

Naraghi, M.E., Javadpour, F., 2015. A stochastic permeability model for the shale-gas systems. Int. J. Coal Geol. 140, 111–124.

Ruppert, L.F., et al., 2013. A USANS/SANS study of the accessibility of pores in the Barnett Shale to methane and water. Energy & Fuels 27 (2), 772–779.

Shaffer, D.L., et al., 2013. Desalination and reuse of high-salinity shale gas produced water: drivers, technologies, and future directions. Environ. Sci. Technol. 47 (17), 9569–9583.

Sheng, G., Su, Y., Wang, W., 2019. A new fractal approach for describing induced-fracture porosity/permeability/compressibility in stimulated unconventional reservoirs. J. Petrol. Sci. Eng. 179, 855–866.

Sheng, M., Li, G., Tian, S., Huang, Z., Chen, L., 2016. A fractal permeability model for shale matrix with multi-scale porous structure. Fractals 24 (1), 1650002.

Tan, X.-H., Jiang, L., Li, X.-P., Zhang, B.-J., Li, X.-C., 2018. Flow model of a multi-stage hydraulic fractured horizontal well based on tree-shaped fractal fracture networks. J. Petrol. Sci. Eng. 169, 494–503.

Tan, Y., et al., 2019. Laboratory characterisation of fracture compressibility for coal and shale gas reservoir rocks: a review. Int. J. Coal Geol. 204, 1–17.

Tian, J., et al., 2019. A dynamic fractal permeability model for heterogeneous coalbed reservoir considering multiphysics and flow regimes. In: SPE/AAPG/SEG Unconventional Resources Technology Conference 2019, URTC 2019.

Vafaie, A., Habibnia, B., Moallemi, S.A., 2015. Experimental investigation of the pore structure characteristics of the Garau gas shale formation in the Lurestan Basin, Iran. J. Nat. Gas Sci. Eng. 27, 432–442.

Wang, D., Yao, J., Chen, Z., Song, W., Sun, H., 2019. Image-based core-scale real gas apparent permeability from pore-scale experimental data in shale reservoirs. Fuel 254, 115596.

Wang, W.-D., Su, Y.-L., Zhang, Q., Xiang, G., Cui, S.-M., 2018. Performance-based fractal fracture model for complex fracture network simulation. Petrol. Sci. 15 (1), 126–134.

Wang, W., Su, Y., Zhang, X., Sheng, G., Ren, L., 2015. Analysis of the complex fracture flow in multiple fractured horizontal wells with the fractal tree-like network models. Fractals 23 (2), 1550014.

Warren, J., Root, P., 1963. The behavior of naturally fractured reservoirs. SPE J. 3 (3), 245–255. Trans., AIME, 228.

Wu, Y.-S., Li, J., Ding, D., Wang, C., Di, Y., 2014. A generalized framework model for the simulation of gas production in unconventional gas reservoirs. SPE J. 19 (5), 845–857.

Wu, Y., et al., 2010. Dual poroelastic response of a coal seam to CO2 injection. International Journal of Greenhouse Gas Control 4 (4), 668–678.

Xu, P., Yu, B., 2008. Developing a new form of permeability and Kozeny–Carman constant for homogeneous porous media by means of fractal geometry. Adv. Water Resour. 31 (1), 74–81.

Xue, X., Yang, C., Onishi, T., King, M.J., Datta-Gupta, A., 2019. Modeling hydraulically fractured shale wells using the fast marching method with local grid refinements LGRs and embedded discrete fracture model EDFM. In: SPE Reservoir Simulation Conference. Society of Petroleum Engineers.

Yaghoubi, A., 2019. Hydraulic fracturing modeling using a discrete fracture network in the Barnett Shale. Int. J. Rock Mech. Min. Sci. 119, 98–108.

Yang, F., Ning, Z., Liu, H., 2014. Fractal characteristics of shales from a shale gas reservoir in the Sichuan Basin, China. Fuel 115, 378–384.

Yang, R., He, S., Yi, J., Hu, Q., 2016. Nano-scale pore structure and fractal dimension of organic-rich Wufeng-Longmaxi shale from Jiaoshiba area, Sichuan Basin: investigations using FE-SEM, gas adsorption and helium pycnometry. Mar. Petrol. Geol. 70, 27–45.

Yu, B., Li, J., 2001. Some fractal characters of porous media. Fractals 9 (3), 365–372.

Yu, W., Luo, Z., Javadpour, F., Varavei, A., Sepehrnoori, K., 2014. Sensitivity analysis of hydraulic fracture geometry in shale gas reservoirs. J. Petrol. Sci. Eng. 113, 1–7.

Yu, W., Sepehrnoori, K., 2014. Simulation of gas desorption and geomechanics effects for unconventional gas reservoirs. Fuel 116, 455–464.

Yuan, B., Zheng, D., Moghanloo, R.G., Wang, K., 2017. A novel integrated workflow for evaluation, optimization, and production predication in shale plays. Int. J. Coal Geol. 180, 18–28.

Zhang, H., Liu, J., Elsworth, D., 2008. How sorption-induced matrix deformation affects gas flow in coal seams: a new FE model. Int. J. Rock Mech. Min. Sci. 45 (8), 1226–1236.

Zhang, J., et al., 2019. Comparative evaluation of the compressibility of middle and high rank coals by different experimental methods. Fuel 245, 39–51.

Zhang, T., Ellis, G.S., Ruppel, S.C., Milliken, K., Yang, R., 2012. Effect of organic-matter type and thermal maturity on methane adsorption in shale-gas systems. Org. Geochem. 47, 120–131.

Zheng, Q., Yu, B., Duan, Y., Fang, Q., 2013. A fractal model for gas slippage factor in porous media in the slip flow regime. Chem. Eng. Sci. 87, 209–215.